

# Multidimensional Infrared Signatures of Intramolecular Hydrogen Bonding in Malonaldehyde

Tomoyuki Hayashi<sup>†</sup> and Shaul Mukamel<sup>\*,†,‡</sup>

Department of Chemistry and Department of Physics and Astronomy, University of Rochester, Rochester, New York 14627-0216

Received: May 15, 2003; In Final Form: July 31, 2003

The sixth-order anharmonic force field of malonaldehyde along the two proton-transfer double-well coordinates and the four O–H and C=O stretching modes is constructed at the MP2/6-31G(d,p) level. The vibrational Hamiltonian is diagonalized using the Arnoldi method. Coherent infrared (IR) vibrational spectra are predicted using the vibrational eigenstates. The three pulse IR signals, calculated in all possible phase matching directions, show specific signatures of the intramolecular proton transfer.

## 1. Introduction

Hydrogen bonding and proton transfer are important in many chemical and biophysical processes. The  $\sim 3300\text{ cm}^{-1}$  O–H infrared (IR) stretch band contains several easily recognizable signatures of hydrogen bonding: a red shift, enhanced intensity, and line broadening.<sup>1,2</sup>

Malonaldehyde (MA) is one of the simplest model systems for intramolecular proton transfer, and its structure and dynamics have been the focus of many experimental and theoretical investigations over the past two decades.<sup>3–12</sup> Microwave spectroscopy done by Wilson's group<sup>3,4</sup> and other researchers<sup>5,6</sup> suggests that proton transfer occurs via tunneling between two O atoms (Figure 1). Centroid transition state theory shows that the quantization of the H atom has a large effect on the transition barrier of the ab initio potential of mean force along the reaction coordinate.<sup>12</sup> The linear infrared (IR) spectrum has been studied;<sup>9–11</sup> however, band assignments based on normal mode calculations are not obvious, because of the tunneling and strong anharmonicities. The tunneling splittings of the vibrational ground state predicted from electronic structure calculations with a one-dimensional (1-D) reaction path model— $1.76 \times 10^{-3}\text{ cm}^{-1}$  (Intrinsic Reaction Coordinate, IRC<sup>13</sup>),<sup>14</sup> or  $0.65\text{ cm}^{-1}$  (shortest path)—which is obtained in this study, do not agree with the experimental value ( $21.6\text{ cm}^{-1}$ ),<sup>7</sup> because of the strong coupling between the tunneling coordinate and other vibrational modes. Therefore, a multicoordinate vibrational Hamiltonian is required to represent the proton-transfer dynamics.

Accurate potential energy surfaces (PESs) have been constructed for smaller molecules. The seventh-order force field with the Morse-transformed coordinates was proposed for water, and the calculated vibrational eigenstates at  $<20\,000\text{ cm}^{-1}$  are reproduced to within a few inverse centimeters.<sup>15</sup> Vibrational and rotational dynamics of water (HOD in liquid D<sub>2</sub>O) were studied semiclassically on this surface<sup>16–18</sup> and found to be in reasonable agreement with hole burning,<sup>19</sup> photon echo,<sup>20,21</sup> and IR pump–probe experiments.<sup>22,23</sup> Quartic multicoordinate model potentials were proposed for the proton transfer in MA<sup>24</sup> and toropolone,<sup>25</sup> in which only anharmonic couplings between a

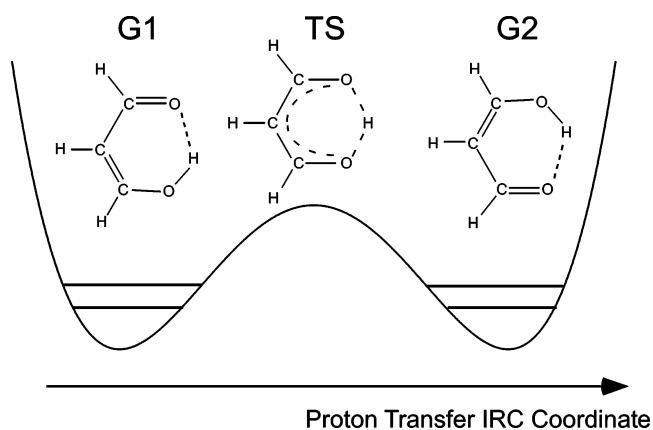


**Figure 1.** One-dimensional (1-D) model of intramolecular proton transfer in malonaldehyde.

single proton-transfer reaction coordinate and the other coordinates are included. In this study, we construct a six-dimensional vibrational Hamiltonian that is based on an ab initio anharmonic force field. Sixth-order anharmonicities in the proton-transfer coordinates and quartic anharmonicities for other coordinates are calculated. We found that the sixth-order force field is necessary to reproduce the anharmonic force constants between the double-well reaction coordinate and the other coordinates.

Several semiclassical studies of the vibrational eigenstates of MA have been performed. The calculated ground-state tunneling splitting from the action integrals of the classical trajectories through the barrier ( $13.9\text{ cm}^{-1}$ ) was determined to be in reasonable agreement with experiment.<sup>14,26</sup> The splitting of other fundamental modes has also been estimated using the perturbative instanton approach.<sup>24</sup> This semiclassical treatment can include all coordinates and was only applied to the low-lying states. Quantum mechanical calculations are limited to handle fewer coordinates and have been applied only to less-anharmonic systems. The vibrational self-consistent field (VSCF) method<sup>27</sup> and its correlation correction version (CC-VSCF)<sup>28</sup> were applied to polyatomic systems, assuming a pairwise additive potential. However, the potential is limited to proton-transfer systems in which three coordinate couplings should be included.<sup>24</sup> The discrete variable representation (DVR)<sup>29,30</sup> and the multiconfigurational time-dependent Hartree (MCTDH)

\* Author to whom correspondence should be addressed. Present address: Department of Chemistry, University of California, Irvine, CA 92697-2025. E-mail: smukamel@uci.edu.

<sup>†</sup> Department of Chemistry.

<sup>‡</sup> Department of Physics and Astronomy.

method<sup>31–33</sup> have been applied to ultrafast laser-driven hydrogen-bonding dynamics in phthalic acid monomethylester (PMME-D),<sup>34,35</sup> which is less anharmonic than MA.

The present study extends the excitonic vibrational Hamiltonian,<sup>36</sup> which uses a harmonic oscillator basis set that corresponds to the local frequencies. We adopt a general harmonic oscillator basis set with an arbitrary frequencies and displacements. With this basis, all matrix elements of the vibrational Hamiltonian that have been expanded as polynomials of coordinates can be calculated analytically, and the excitonic description is more accurate than the DVR method. The Implicit Restated Arnoldi Method (IRAM) is used for the diagonalization of the large Hamiltonian matrix. The typical dimension size is  $\sim 10^5$ – $10^6$ .

The O–H stretch with a strong hydrogen bond has an extremely broad ( $500\text{ cm}^{-1}$ ) bandwidth, which complicates the microscopic analysis of the IR spectra. Three pulse nonlinear IR spectroscopies provide detailed information on molecular structures by spreading the spectroscopic information in two dimensions, selectively eliminating certain static broadening mechanisms, and providing ultrafast structural and dynamical information unavailable from 1-D linear measurements.<sup>37–42</sup> These techniques should provide a powerful tool for exploring the structure and proton-transfer dynamics in hydrogen-bonded systems.

We have simulated the three pulse nonlinear IR signals generated at the four possible signal wavevectors. To identify the signatures of proton transfer, the signals calculated for the double-well (DW) potential are compared with a single-well (SW) model potential, where proton transfer is prohibited. Several new off-diagonal cross peaks are found in the DW potential. These peaks, which are induced by intramolecular proton transfer, are assigned to the Liouville space paths which include the transitions between the O–H stretch fundamental and second-order or higher harmonics, which have much lower frequencies than expected in a harmonic system, because of the strong mixing with the proton-transfer reaction coordinate.

## 2. Reaction Coordinates and the Ab Initio Force Field

IR spectra<sup>9,10</sup> show that MA is planar. Proton transfer occurs in two equivalent *cis*-enol isomers (G1 and G2) with  $C_s$  point group symmetry, whereas the transition state (TS) ( $C_{2v}$  symmetry) connects the G1 and G2 isomers (see Figure 1).

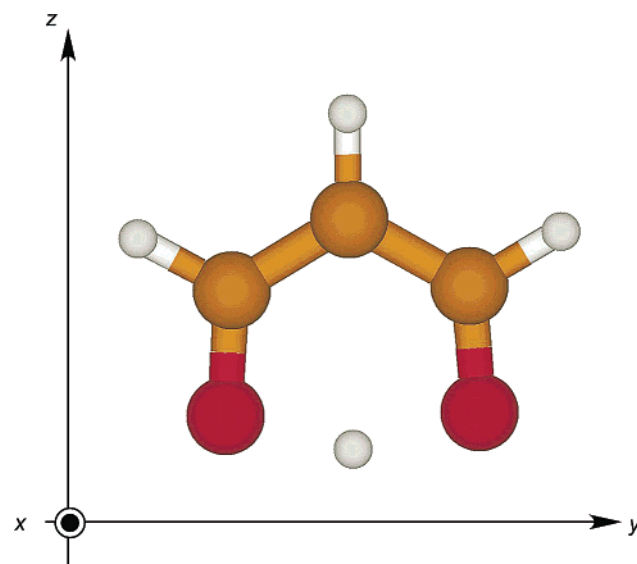
B3LYP/6-31G(d,p), MP2/6-31G(d,p), QCISD/6-31G(d,p), and CCD/6-31G(d,p) levels were used in the present study to locate the structures of G1, G2, and TS, using Gaussian98.<sup>43</sup> The barrier heights for proton transfer ( $\Delta E \equiv E_{\text{TS}} - E_{\text{G1,2}}$ ) were determined to be  $831\text{ cm}^{-1}$  (B3LYP),  $1199\text{ cm}^{-1}$  (MP2),  $2161\text{ cm}^{-1}$  (QCISD), and  $2382\text{ cm}^{-1}$  (CCD). Compared to the upper bound that has been determined from the <sup>1</sup>H NMR studies ( $2134\text{ cm}^{-1}$ ),<sup>8</sup> the B3LYP and MP2 levels underestimate the barrier and the QCISD and CCD levels overestimate it. The high CCSD(T) level provides a reasonable estimate of the barrier height,  $1504\text{ cm}^{-1}$ .<sup>44</sup> The CCSD(T) or QCISD(T) level was also required in the similar H-atom transfer system of formimidol.<sup>45</sup> Triple excitations are crucial for reproducing the barrier height. The basis-set dependence of the barrier at the MP2 level was investigated in ref 14, and no significant improvements were observed with the larger basis set. The MP2/6-31G(d,p) level was used in all our subsequent calculations.

Table 1 shows the normal modes of MA in the G1 and G2 geometries. Both O–H and C=O stretch have strong IR intensities. Because their bond lengths are affected by the proton transfer,<sup>14</sup> the nonlinear IR bands of these vibrational modes

**TABLE 1: Normal Modes of Malonaldehyde with Large Infrared Intensities in the G1 and G2 Configurations, Calculated at the MP2/6-31(d,p) Level<sup>a</sup>**

mode	description	frequency ( $\text{cm}^{-1}$ )	IR intensity
6	ring deformation	895.4	medium
12	C–O stretch	1310.1	medium
16	H–O–C bend	1683.4	strong
17	C=O stretch	1736.8	strong
18	C–H <sub>γ</sub> stretch	3088.3	medium
20	O–H stretch	3319.9	medium

<sup>a</sup> The normal modes are indexed with increasing frequency.



**Figure 2.** Calculated structure of the reference geometry. The  $x$ -,  $y$ -, and  $z$ -axes shown here will be used in Table 6. Malonaldehyde is on the  $y$ - $z$  plane, and the  $x$ -axis is in perpendicular.

are expected to be markers for the energy surface along the proton-transfer coordinate.

The IRC<sup>13</sup> path, which connects the two energy minima G1 and G2, is described by the path within the two-dimensional (2-D) configurational space<sup>14</sup> (which is referenced as a reaction plane) that includes three configurations  $\xi_{\text{G1}}$ ,  $\xi_{\text{G2}}$ , and  $\xi_{\text{TS}}$ , with two basis vectors,  $\xi'_1 \equiv \xi_{\text{G1}} - \xi_{\text{G2}}$  and  $\xi'_2 \equiv \xi_{\text{TS}} - \xi_0$ , where  $\xi_A$  denotes  $3N$  mass-weighted Cartesian coordinates for the configuration A ( $A = \text{G1}, \text{G2}, \text{TS}$ ).  $\xi'_1$  is a least-motion path that connects  $\xi_{\text{G1}}$  and  $\xi_{\text{G2}}$ , and  $\xi_0$  is defined as  $\xi_0 \equiv (\xi_{\text{G1}} + \xi_{\text{G2}})/2$ . The calculated structure of the reference geometry  $\xi_0$  is shown in Figure 2.

Our six-dimensional configurational space is made of the two reaction basis vectors  $\xi'_1$  and  $\xi'_2$ , together with the following symmetric and antisymmetric four basis vectors that represent the O–H and C=O stretching modes of G1 and G2:

$$\xi'_3 = \frac{1}{\sqrt{2}}(\xi_{17}^{\text{G1}} + \xi_{17}^{\text{G2}}) \quad (1a)$$

$$\xi'_4 = \frac{1}{\sqrt{2}}(\xi_{17}^{\text{G1}} - \xi_{17}^{\text{G2}}) \quad (1b)$$

$$\xi'_5 = \frac{1}{\sqrt{2}}(\xi_{20}^{\text{G1}} + \xi_{20}^{\text{G2}}) \quad (2a)$$

$$\xi'_6 = \frac{1}{\sqrt{2}}(\xi_{20}^{\text{G1}} - \xi_{20}^{\text{G2}}) \quad (2b)$$

Here,  $\xi_n^A$  represents the mass-weighted Cartesian displacement vector of mode  $n$  in the geometry A. These six basis vectors

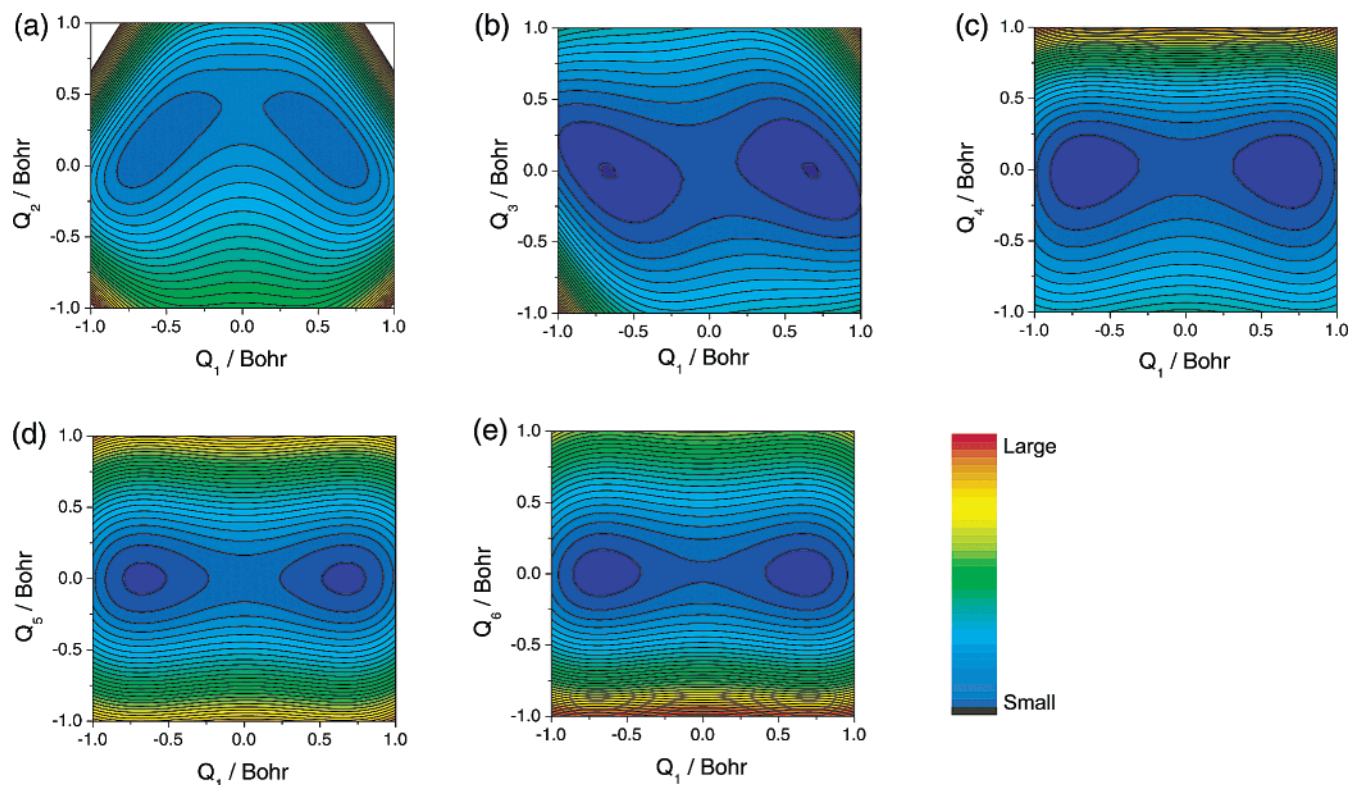


**Figure 3.** Potential energy surfaces (PESs) projected onto two-dimensional (2-D) space spanned by  $Q_1$  and five other coordinates ( $Q_2$ , the other reaction coordinate;  $Q_3$ , O–H stretch in  $B_2$  symmetry;  $Q_4$ , O–H stretch in  $A_1$  symmetry;  $Q_5$ , C=O stretch in  $B_2$  symmetry; and  $Q_6$ , C=O stretch in  $A_1$  symmetry). The PES spanned by  $Q_1$  and the coordinates in  $A_1$  symmetry (panels a, c, and e) have line symmetry, and the PES on the  $Q_1$  and the coordinates in  $B_2$  symmetry (panels b and d) have point symmetry. Panel a shows the PES on the reaction plane, which corresponds to Figure 4 in ref 14. Anharmonic couplings between  $Q_1$  and the O–H stretch (panels b and c) are larger than that between  $Q_1$  and the C=O stretch (panels d and e).

were subject to normalization and Gram–Schmidt orthogonalization<sup>46</sup> (see Appendix A), resulting in our final orthonormal basis vectors  $\xi_1 \cdots \xi_6$  and corresponding coordinates  $Q_1, \dots, Q_6$ .  $\xi_1$  and  $\xi_2$  are the normalized  $\xi'_1$  and  $\xi'_2$  parameters. We therefore denote  $Q_1$  and  $Q_2$  as reaction coordinates 1 (RC1) and 2 (RC2), respectively.  $\xi_3$  is a combination of  $\xi'_1$  and  $\xi'_3$ .  $\xi_5$  is a combination of  $\xi'_1$ ,  $\xi'_3$ , and  $\xi'_5$ .  $\xi_4$  is a combination of  $\xi'_2$  and  $\xi'_4$ .  $\xi_6$  is a linear combination of  $\xi'_2$ ,  $\xi'_4$ , and  $\xi'_6$ .

The ab initio potential energy surface ( $V$ ) was expanded around the reference geometry  $\xi_0$  to sixth order in our six orthonormal coordinates  $Q_k$ :

$$\mathcal{H} = \sum_i \frac{P_i^2}{2m_i} + \sum_i f_i^{(1)} Q_i + \sum_{ij} f_{ij}^{(2)} Q_i Q_j + \sum_{ijk} f_{ijk}^{(3)} Q_i Q_j Q_k + \sum_{ijkl} f_{ijkl}^{(4)} Q_i Q_j Q_k Q_l + \sum_{ijklm} f_{ijklm}^{(5)} Q_i Q_j Q_k Q_l Q_m + \sum_{ijklm,n} f_{ijklm,n}^{(6)} Q_i Q_j Q_k Q_l Q_m Q_n \quad (3)$$

where

$$f_{i_1 \cdots i_n}^{(n)} = \frac{1}{n!} \left( \frac{\partial^n V}{\partial Q_{i_1} \cdots \partial Q_{i_n}} \right)_{\text{eq}} \quad (4)$$

The small coefficients  $f^{(4)}$ , which depend on four different coordinates, were neglected. In the fifth and sixth orders, we retained only the largest terms:  $f_{ij111}^{(5)}$  and  $f_{ij1111}^{(6)}$ . The terms  $f_{ij1}^{(3)}$  to  $f_{ij1111}^{(6)}$ , which include coordinate  $Q_1$ , were determined nu-

merically by calculating up to fourth-order derivatives of analytical quadratic force constants  $f_{ij}^{(2)}$ , with respect to coordinate  $Q_1$ , using five-point central difference formulas (see Appendix B). The other anharmonic force constants were determined by calculating first and second derivatives of analytic quadratic force constants with three-point central difference formulas.<sup>47</sup> The two displacement steps of  $Q_1$  for the five-point difference formula are set to  $\delta_1 = 0.2 \text{ \AA}$  and  $\delta_2 = 0.375 \text{ \AA}$ , and the displaced geometries with  $\delta_2$  correspond to the two equilibrium geometries  $\xi_{G1}$  and  $\xi_{G2}$ . The displacements  $\delta$  of all the other coordinates for the three-point difference formula are set as  $0.01 \text{ \AA}$ . The quadratic force constants in the orthonormal coordinates were obtained from the analytic quadratic force constants in Cartesian coordinates that have been calculated with Gaussian98.

We estimated the numerical error by comparing the cubic force constants with the permutation of the three indices  $f_{ijk}^{(3)}$ ,  $f_{jki}^{(3)}$ , and  $f_{kij}^{(3)}$ . The force constants that included  $Q_1$  varied by <10% (300% if the quartic force field were applied, using the three-point difference formula). The three values are within 1% for all the other cubic force constants that exclude  $Q_1$ . Thus, the sixth-order force field is necessary to model the energy surface. The force field was scaled on one parameter (the square of the ratio of the distance between the G1 and G2 geometries to the amplitude of zero-point vibrations of RC1 at G1) given in ref 24 to reproduce the experimental tunneling splitting of the ground state. The calculated anharmonic force constants with  $Q_1$ ,  $Q_2$ , and  $Q_3$  are shown in Table 2. Because of the two equivalent hydrogen-bonded structures (Figure 1), the 1-D potential along  $Q_1$  is a symmetric double well, i.e.,  $f_1^{(1)} = 0$ ,  $f_{11}^{(2)} < 0$ ,  $f_{111}^{(3)} = 0$ ,  $f_{1111}^{(4)} > 0$ ,  $f_{11111}^{(5)} = 0$ , and  $f_{111111}^{(6)} > 0$ .

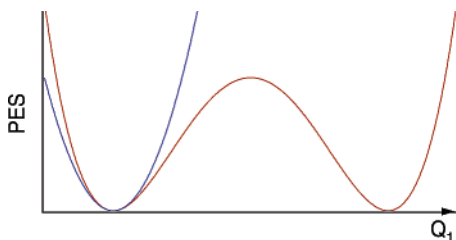


**Figure 4.** Plot showing that the double-well (DW) potential energy curve along the  $Q_1$  (red line) is replaced by the single-well (SW) harmonic potential (blue line) in the SW model potential; the SW potential curve has the same frequency as the DW potential curve at geometry G1.

**TABLE 2: Calculated Anharmonic Force Constants<sup>a</sup> with  $Q_1$ ,  $Q_2$ , and  $Q_3$**

parameter	calculation	parameter	calculation
$f_1^{(1)}$	0.0000	$f_{1111}^{(4)}$	0.0757
$f_2^{(1)}$	-0.0557	$f_{1112}^{(4)}$	0.0000
$f_3^{(1)}$	0.0000	$f_{1113}^{(4)}$	0.0342
$f_{11}^{(2)}$	-0.0830	$f_{1122}^{(4)}$	0.0138
$f_{12}^{(2)}$	0.0000	$f_{1123}^{(4)}$	0.0000
$f_{13}^{(2)}$	-0.0409	$f_{1133}^{(4)}$	0.0158
$f_{22}^{(2)}$	0.0432	$f_{1222}^{(4)}$	0.0000
$f_{23}^{(2)}$	0.0000	$f_{1223}^{(4)}$	0.0088
$f_{33}^{(2)}$	0.1049	$f_{1233}^{(4)}$	0.0000
$f_{11}^{(3)}$	0.0000	$f_{1333}^{(4)}$	0.0091
$f_{112}^{(3)}$	0.0149	$f_{2222}^{(4)}$	0.0098
$f_{113}^{(3)}$	0.0000	$f_{2223}^{(4)}$	0.0000
$f_{122}^{(3)}$	0.0000	$f_{2233}^{(4)}$	0.0039
$f_{123}^{(3)}$	0.0087	$f_{2333}^{(4)}$	0.0000
$f_{133}^{(3)}$	0.0000	$f_{3333}^{(4)}$	0.0118
$f_{222}^{(3)}$	0.0257	$f_{11111}^{(5)}$	0.0000
$f_{223}^{(3)}$	0.0000	$f_{11211}^{(5)}$	0.0132
$f_{233}^{(3)}$	0.0047	$f_{11311}^{(5)}$	0.0000
$f_{333}^{(3)}$	0.0000	$f_{12211}^{(5)}$	0.0000
		$f_{12311}^{(5)}$	0.0080
		$f_{13311}^{(5)}$	0.0000
		$f_{111111}^{(6)}$	0.0051
		$f_{112111}^{(6)}$	0.0000
		$f_{113111}^{(6)}$	0.0061
		$f_{122111}^{(6)}$	0.0080
		$f_{123111}^{(6)}$	0.0000
		$f_{133111}^{(6)}$	0.0045

<sup>a</sup> Expressed in terms of hartree·bohr<sup>-n</sup>.

The PESs projected onto the 2-D space spanned by  $Q_1$  and each of the five other coordinates are displayed in Figure 3. ( $Q_1$ ,  $Q_2$ ) is the reaction plane, and the PESs projected onto this space are identical to those obtained with the modified Shepard interpolation method by Hirao et al.<sup>14</sup>  $Q_3$  and  $Q_6$  have  $B_2$  symmetry, and the PESs spanned by them together with  $Q_1$  show the antisymmetric mode coupling (ASMC) shape,<sup>25</sup> which has point symmetry, whereas  $Q_2$ ,  $Q_4$ , and  $Q_5$  have  $A_1$  symmetry and the PESs spanned by them together with  $Q_1$  show the symmetric mode coupling (SMC) shape,<sup>25</sup> which has line symmetry. The anharmonic couplings between  $Q_1$  and the O–H stretch modes ( $Q_3$  and  $Q_4$ ) are larger than those with C=O stretches ( $Q_5$  and  $Q_6$ ). This ab initio force field was used in our calculations.

To identify signatures of proton transfer in multidimensional IR signals, we constructed a single-well (SW) model potential

**TABLE 3: Single-Degree-of-Freedom Harmonic Oscillator Basis Functions Assigned to Each Coordinate of the DW and SW Potentials**

mode	frequency (cm <sup>-1</sup> )	mass (a.u.)	number of basis	center position (bohr)
$Q_1$	1748.9	1.44	16	0.0
$Q_2$	499.8	9.13	8	0.1
$Q_3$	1830.3	1.66	6	0.0
$Q_4$	2995.2	1.06	6	0.0
$Q_5$	1535.5	5.95	4	0.0
$Q_6$	1716.4	5.13	4	0.0

**TABLE 4: Calculated Vibrational Eigenstates with Strong IR Intensities to the Split Two Ground States**

index	eigenstates		IR intensity <sup>a</sup> (a.u.)	
	frequency (cm <sup>-1</sup> )	description	1	2
1	0.0	S, ground state		
2	25.6	A, ground state	4.03	
9	1511.9		0.73	0.15
10	1537.7		0.13	0.46
11	1642.6		0.18	0.03
12	1695.3		0.07	0.01
13	1732.9	S,C=O( $\nu=1$ )	0.97	0.22
14	1750.0	A,C=O( $\nu=1$ )	0.23	1.00
15	1916.1		0.04	0.37
22	2339.6	S,O–H( $\nu=1$ )	0.00	0.86
25	2491.8	A,O–H( $\nu=1$ )	1.00	0.00

<sup>a</sup> IR intensities from the two ground states G1 and G2.

where the proton transfer is blocked and the MA is always in G1 geometry.  $f_{1111}^{(4)}$  and  $f_{111111}^{(6)}$  are set as zero and  $f_{11}^{(1)}$  and  $f_{11}^{(2)}$  have the same harmonic frequency as that of the original potential at the G1 geometry (Figure 4). All other force constants are unchanged. Figure 5 shows the 2-D surface spanned by  $Q_1$  and the two other coordinates ( $Q_2$ ,  $Q_3$ ) for this SW model potential. Compared to Figure 3, the local structure of the PES around G1 is preserved, but the second minimum G2 is eliminated. We shall denote these potentials as double-well (DW) and single-well (SW), respectively.

### 3. The Vibrational Eigenstates

Moran et al.<sup>36</sup> used the Hartree product of the single-degree-of-freedom harmonic oscillator eigenfunction as a basis set. The frequency of the basis was equal to the frequency of that mode, and the center position is equal to the origin of the coordinate. However, for a double well, the intrinsic frequency of that mode becomes negative. Therefore, we have extended the approach to use arbitrarily chosen single harmonic oscillator eigenfunctions with arbitrary center positions and eigenfrequencies that are not related to the intrinsic frequencies. The vibrational wave functions were expanded as

$$|\psi\rangle = \sum_{n_{A_1,\omega_1}} \cdots \sum_{n_{A_6,\omega_6}} |n_{A_1,\omega_1}, \cdots, n_{A_6,\omega_6}\rangle \langle n_{A_1,\omega_1}, \cdots, n_{A_6,\omega_6} | \psi \rangle \quad (5)$$

The basis set  $|n_{A_1,\omega_1}, \cdots, n_{A_6,\omega_6}\rangle$  is a Hartree product of the harmonic oscillator potential with an arbitrary center position  $A_i$  and an arbitrary frequency  $\omega_i$ :

$$|n_{A_1,\omega_1}, \cdots, n_{A_6,\omega_6}\rangle \equiv |n_{A_1,\omega_1}\rangle |n_{A_2,\omega_2}\rangle \cdots |n_{A_n,\omega_n}\rangle \quad (6)$$

where  $n$  denotes the number of vibrational quanta in each mode.

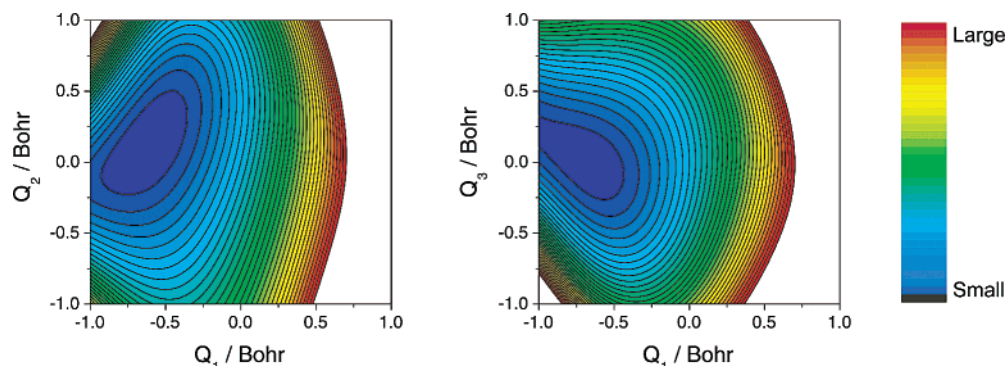


**Figure 5.** PESs of the SW model potential projected onto 2-D space spanned by  $Q_1$  and two other coordinates ( $Q_2$ , the other reaction coordinate; and  $Q_3$ , the O–H stretch in  $B_2$  symmetry); the shape of the PES around geometry G1 is well preserved, compared to the corresponding PESs in Figure 3.

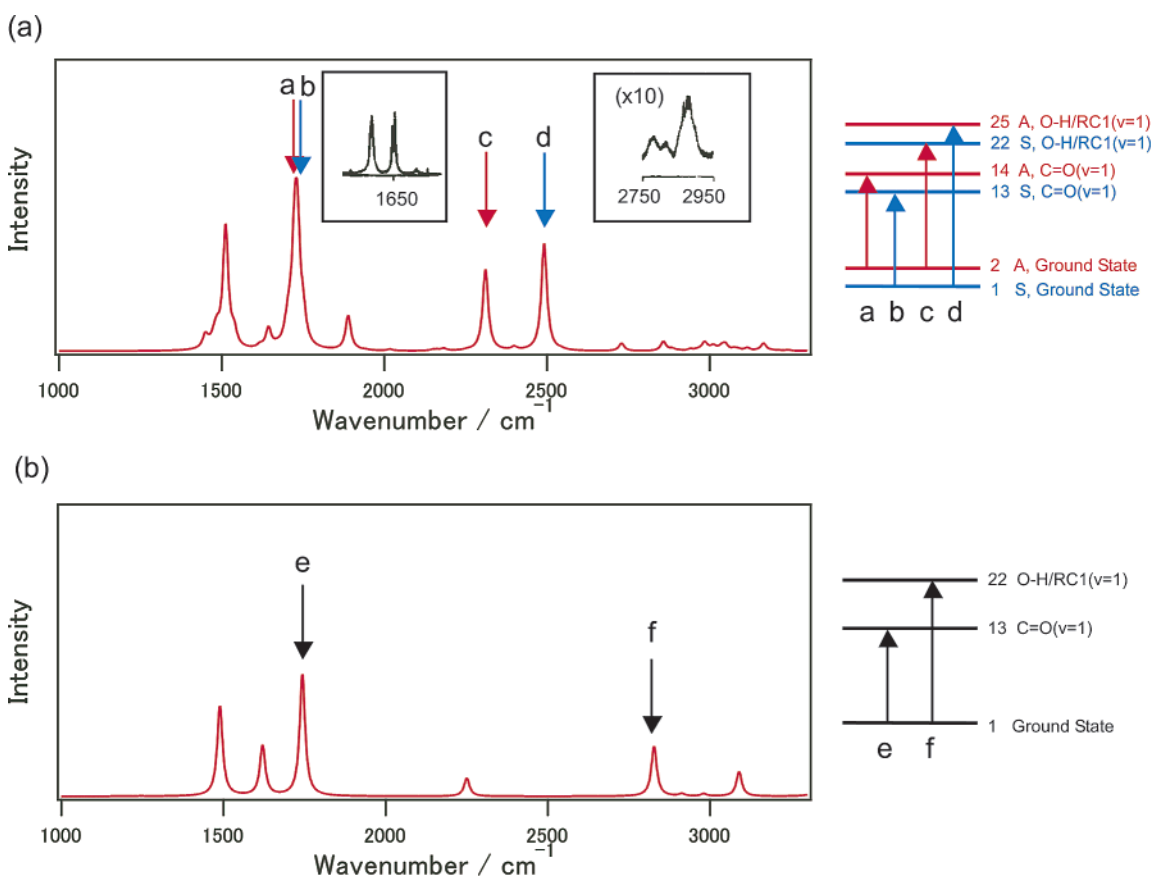


**Figure 6.** Calculated and observed linear infrared (IR) spectra of MA: (a) double well (DW) and (b) single well (SW). The room-temperature (297 K) Boltzman distribution was assumed for eigenstates 1 and 2 in the DW calculation. The experimental IR spectra isolated in a xenon matrix<sup>11</sup> are superimposed on the DW calculation. Energy-level scheme and peak assignments are shown on the right-hand side.

The coordinates  $Q_i$  and momenta  $P_i$  were replaced by bosonic creation ( $B_i^+$ ) and annihilation ( $B_i$ ) operators:

$$Q_i = \sqrt{\frac{\hbar}{2m_i\omega_i}}(B_i^+ + B_i) \quad (7)$$

$$P_i = i\sqrt{\frac{m_i\hbar\omega_i}{2}}(B_i^+ - B_i) \quad (8)$$

Using the Bose commutation relation between  $B_i^+$  and  $B_i$ , and neglecting constant terms, the vibrational Hamiltonian in a normally ordered form is given in Appendix C.

The harmonic oscillator basis functions used for each coordinate are summarized in Table 3. High-energy basis states, where the total number of excitations ( $n_T = \sum n_{A,\omega_i}$ ) is large,

only weakly affect the energy levels of lower-lying eigenstates. Therefore, basis states with  $n_T > 36$  were neglected. The total number of basis states is 73 728 (DW), and IRAM was used to solve the large-scale eigenvalue problem. The Arnoldi subroutine was taken from the public domain ARPACK package.<sup>48–50</sup> All 245 DW states that lie below 6000  $\text{cm}^{-1}$  were included in the simulation. The transition dipole moment between the eigenstates was calculated from the dipole moment derivative, with respect to the mass-weighted normal coordinates.<sup>36</sup>

#### 4. Linear Infrared Spectra

The calculated room-temperature (297 K) linear IR spectra for the DW and SW potentials are displayed in Figure 6 and compared with experiment.<sup>11</sup> A homogeneous line width of 10  $\text{cm}^{-1}$  was assumed for all transitions. The calculated vibrational

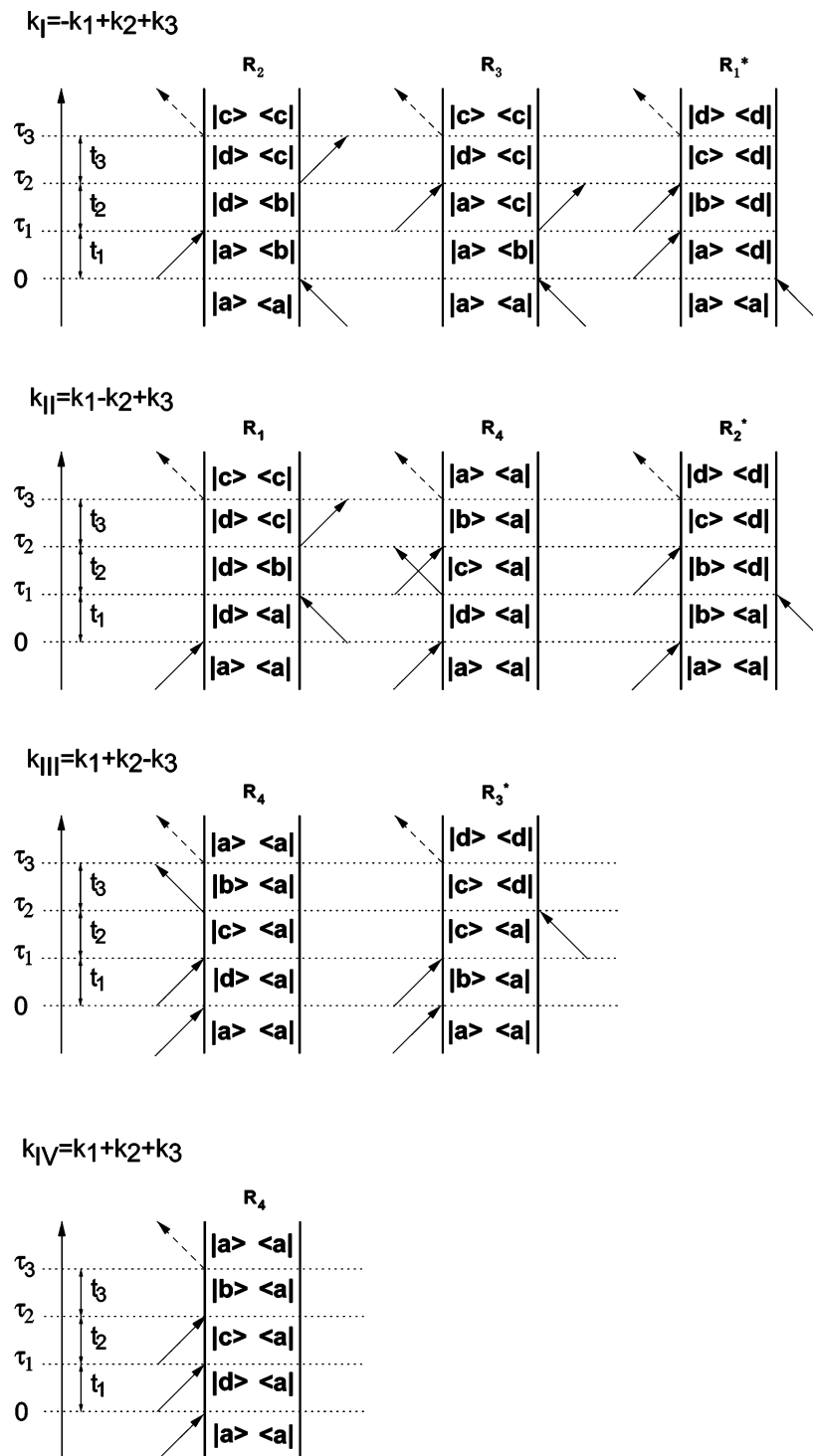


**Figure 7.** Double-sided Feynman diagrams describing the third-order response in four possible directions as indicated; the resonant diagrams with RWA approximation in this calculation are shown.

eigenstates with strong IR intensities to the split two ground states are summarized in Table 4. The states are ordered by increasing frequency. Each vibrational state for the double well is split into two components, symmetric and antisymmetric, which represent the tunneling. The calculated ground-state splitting ( $25.7 \text{ cm}^{-1}$ ) is in excellent agreement with microwave measurements ( $21.6 \text{ cm}^{-1}$ ). We also calculated the splitting that included only one reaction coordinate  $Q_1$  (RC1), with  $n_T = 36$ , which resulted in a value of  $0.65 \text{ cm}^{-1}$ . The increase of the splitting with the extra coordinates  $Q_2, \dots, Q_6$  is attributed to the strong coupling between RC1 and the other coordinates.

The calculated DW spectra capture the qualitative characters of the O–H and C=O stretch peaks. In the  $2750\text{--}2950 \text{ cm}^{-1}$  region, experiments show a medium peak at  $\sim 2860 \text{ cm}^{-1}$  and one smaller peak at  $2777 \text{ cm}^{-1}$ , neither of which were assigned in the previous study.<sup>11</sup> The DW calculation reproduces these two peaks. The calculated peak at  $2491.8 \text{ cm}^{-1}$  is assigned to the transition from the symmetric (S) ground state to antisymmetric (A), O–H ( $\nu = 1$ ), or A, O–H/RC1 ( $\nu = 1$ ), which explicitly indicates the mixing of the O–H stretch and RC1. The  $2314.0 \text{ cm}^{-1}$  peak corresponds to the transition from the antisymmetric (A) ground state to symmetric (S) O–H/RC1 ( $\nu = 1$ ). The calculated tunneling splitting of  $152.2 \text{ cm}^{-1}$  for the

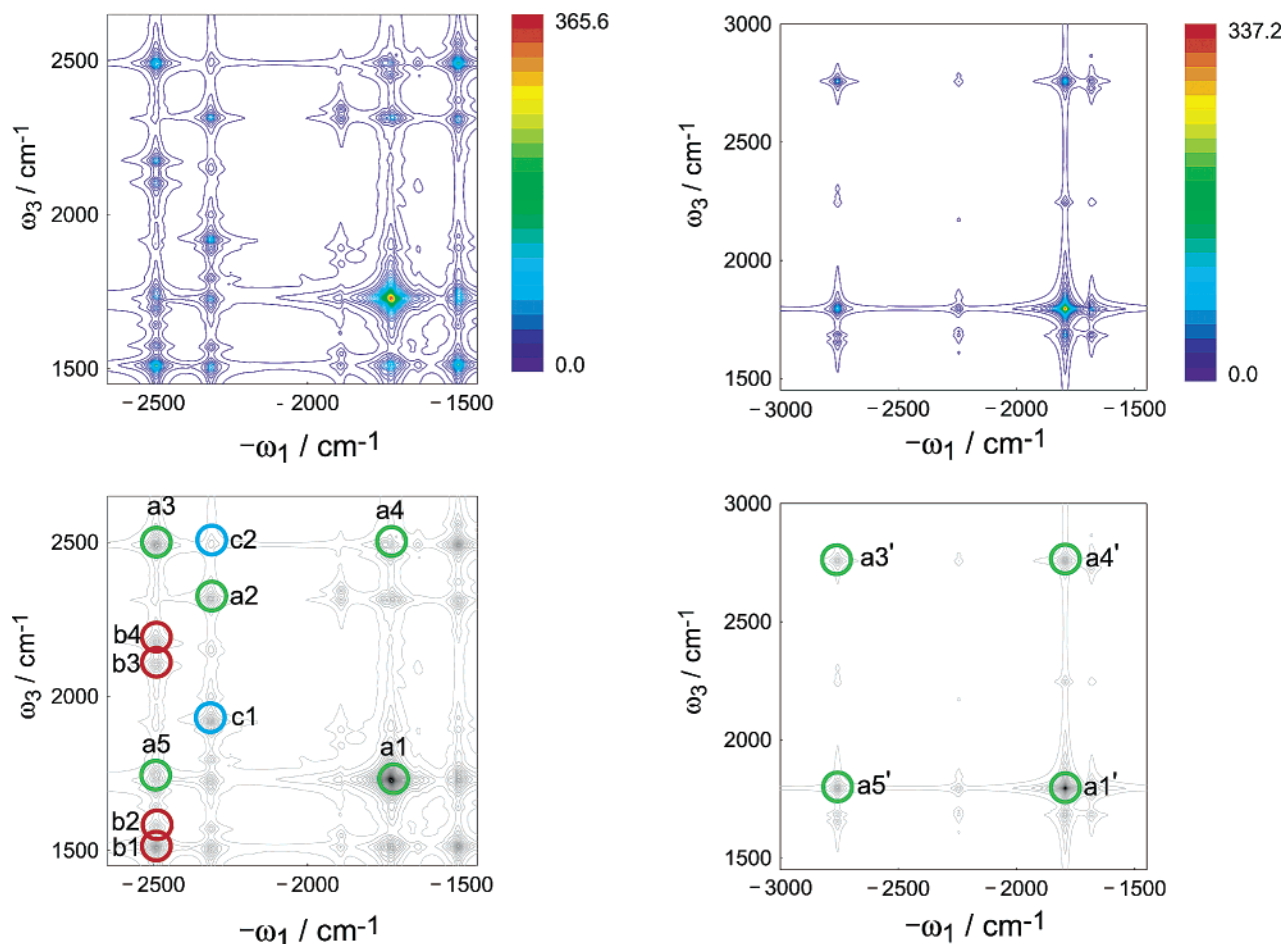


**Figure 8.** Three-pulse  $\mathbf{k}_I$  signal (absolute value of  $S(-\omega_1, t_2 = 0, \omega_3)$  in eq 13) of MA. The three incident pulses (10 fs) are tuned to  $2200 \text{ cm}^{-1}$  and have a bandwidth of  $\pm 700 \text{ cm}^{-1}$  (left) DW model data and (right) SW model data. Top figures are the signals, and bottom figures highlight the main peaks with colored circles and denotations. Peaks with red and blue circles in the DW signal are originating from the Liouville space paths that involve transitions from the A,C=O/RC1( $v = 1$ ) and S,C=O/RC1( $v = 1$ ) states to higher excited states, respectively. Remaining peaks are marked with green circles. The Liouville space paths of the peaks are shown in Figures 9 and 10.

O–H stretch agrees reasonably well with the estimated experimental tunneling splitting, which was  $105 \text{ cm}^{-1}$  ( $2860 \text{ cm}^{-1} - 2777 \text{ cm}^{-1} + 21.6 \text{ cm}^{-1} = 105 \text{ cm}^{-1}$ ). Note that the calculated relative intensities of the two peaks are different from experimental values because the assumed room temperature is much higher than the experimental temperature (10 K). The 35 K simulation is in good agreement with experiment. Room temperature was used to study the peaks that involve transitions from the second ground state. The intense experimental peak at  $1650 \text{ cm}^{-1}$  is assigned to the C=O stretch fundamental. According to the DW calculation, this is comprised of two degenerate peaks: one is assigned to the transition from the S ground state to symmetric C=O( $v = 1$ ), and the other is assigned to the transition from the A ground state to antisymmetric C=O/RC1( $v = 1$ ). The calculated splitting of C=O stretch is  $17.1 \text{ cm}^{-1}$ , which also agrees well with the experiment ( $1650 \text{ cm}^{-1} - 1650 \text{ cm}^{-1} + 21.6 \text{ cm}^{-1} = 22 \text{ cm}^{-1}$ ).

Comparison of the SW and DW calculations shows that the O–H stretch fundamental is red-shifted from  $2828 \text{ cm}^{-1}$  (SW) to  $2491 \text{ cm}^{-1}$  (DW). In contrast, the C=O stretch fundamental is hardly affected:  $1743 \text{ cm}^{-1}$  (SW) and  $1750 \text{ cm}^{-1}$  (DW). The red shift of the O–H stretch is typical in hydrogen bonding. Our calculations suggest that the red shift is related to the proton transfer due to the other potential minimum G2.

Quantitatively, the calculated peak position of the C=O stretch is satisfactory; however, the calculated O–H stretch is  $359 \text{ cm}^{-1}$  less than the experimental value. This frequency is

very sensitive to the proton-transfer barrier, and this difference may attributed to the limited accuracy of the ab initio calculation. The calculated spectra reproduce the peaks related to the C=O and O–H normal modes, which are responsible for the most prominent signatures of proton transfer in linear and 2-D IR spectra. Other spectral regions may be calculated in the same way. This goes beyond the scope of the present study.

### 5. Three Pulse Nonlinear Infrared Signals

We have calculated the three pulse IR signals of MA generated in the four possible directions:  $\mathbf{k}_I = -\mathbf{k}_1 + \mathbf{k}_2 + \mathbf{k}_3$ ,  $\mathbf{k}_{II} = \mathbf{k}_1 - \mathbf{k}_2 + \mathbf{k}_3$ ,  $\mathbf{k}_{III} = \mathbf{k}_1 + \mathbf{k}_2 - \mathbf{k}_3$ , and  $\mathbf{k}_{IV} = \mathbf{k}_1 + \mathbf{k}_2 + \mathbf{k}_3$  with ZZZZ polarization using the sum-over-states expression<sup>51</sup> and orientational factors taken from eq 13 in the work of Hochstrasser.<sup>52</sup> Signals were calculated for both the DW and SW potentials, to reveal the effect of proton transfer on the signals.

Using the rotating wave approximation (RWA), the response function for each signal is given by the sum of the following Liouville space pathways:

$$R_I(t_3, t_2, t_1) = R_2(t_3, t_2, t_1) + R_3(t_3, t_2, t_1) - R_1^*(t_3, t_2, t_1) \quad (9)$$

$$R_{II}(t_3, t_2, t_1) = R_1(t_3, t_2, t_1) + R_4(t_3, t_2, t_1) - R_2^*(t_3, t_2, t_1) \quad (10)$$

$$R_{III}(t_3, t_2, t_1) = R_4(t_3, t_2, t_1) - R_3^*(t_3, t_2, t_1) \quad (11)$$

$$R_{IV}(t_3, t_2, t_1) = R_4(t_3, t_2, t_1) \quad (12)$$

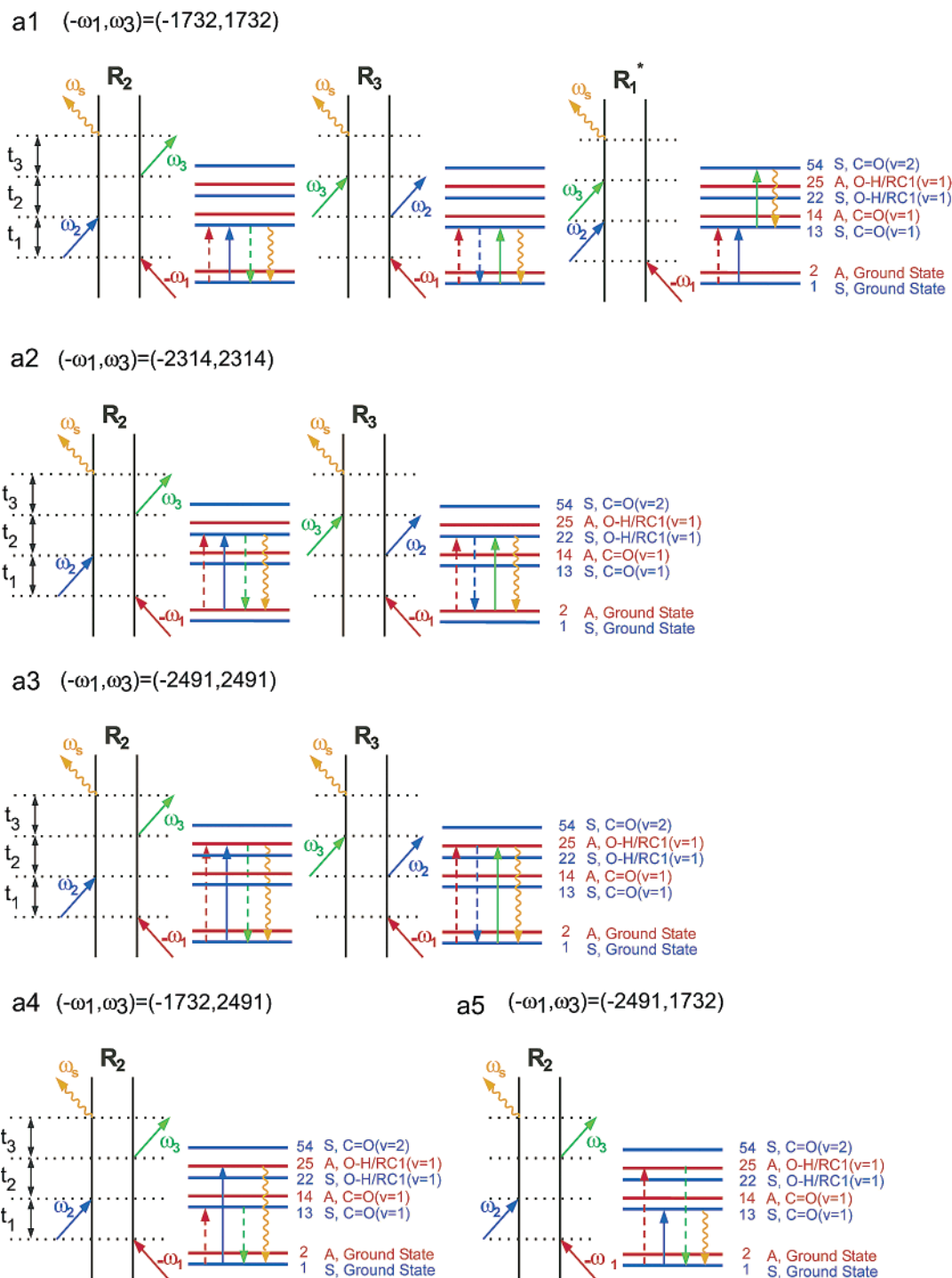


**Figure 9.** Feynman diagrams and energy-level schemes of the main peaks in  $\mathbf{k}_I$  signals of the DW potential. (I)

The Liouville space paths are represented by the double-sided Feynman diagrams given in Figure 7, where  $a$ ,  $b$ ,  $c$ , and  $d$  correspond to one of the vibrational eigenstates.  $R_S$  (with  $S = \text{I, II, III, IV}$ ) are proportional to the product of the transition dipole moments related to four optical transitions,  $\mu_{ab}\mu_{bc}\mu_{cd}\mu_{da}$ .<sup>53</sup> Using a 2-D Fourier transform with respect to  $t_1$  and  $t_3$ , the  $(\omega_1, \omega_3)$  signal is

$$S(\omega_1, t_2, \omega_3) = \left| \int_{-\infty}^{\infty} dt_3 \int_{-\infty}^{\infty} dt_1 R_S(t_3, t_2, t_1) \exp[-i(\omega_3 t_3 + \omega_1 t_1)] \right| \quad (13)$$

We also calculated an  $(\omega_2, \omega_3)$  signal:

$$S(t_1, \omega_2, \omega_3) = \left| \int_{-\infty}^{\infty} dt_3 \int_{-\infty}^{\infty} dt_2 R_S(t_3, t_2, t_1) \exp[-i(\omega_3 t_3 + \omega_2 t_2)] \right| \quad (14)$$

**5.1. The  $\mathbf{k}_I$  Signal.** The three incident pulses (10 fs) are tuned to  $2200 \text{ cm}^{-1}$ . To obtain the global pattern of 2-D signals at one time, a very broad rectangular bandwidth of  $\pm 700 \text{ cm}^{-1}$  is assumed for each of the three pulses; thus, all energy levels within  $\bar{\omega}_n \pm 700 \text{ cm}^{-1}$  are resonant with the carrier frequency  $\bar{\omega}_n$ . This resulted in a total of 55 347 terms contributing to the

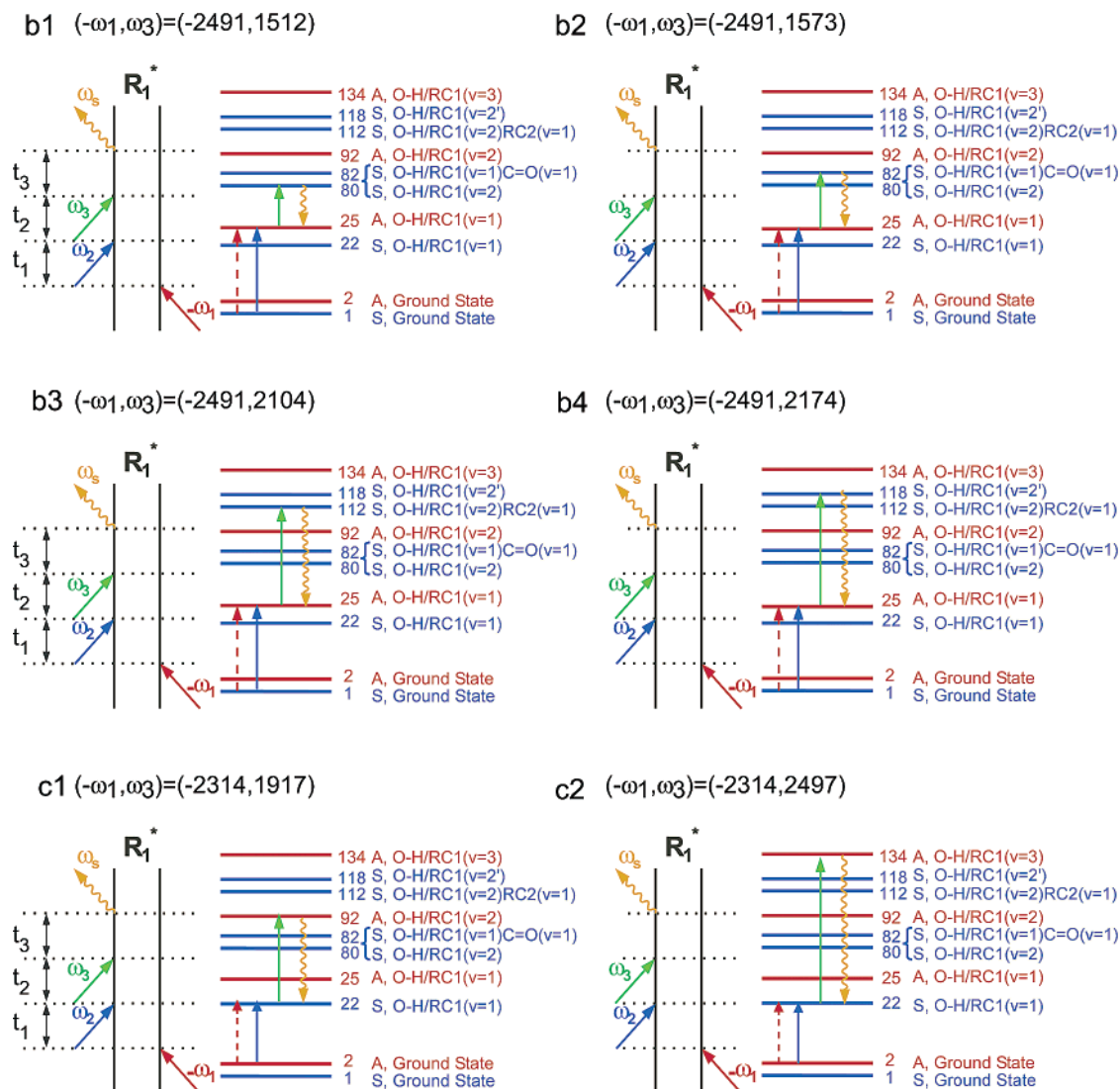


Figure 10. Feynman diagrams and energy-level schemes of the main peaks in  $\mathbf{k}_I$  signals of the DW potential. (II)

TABLE 5: Vibrational Eigenstates Involved in the Liouville Space Paths that Contribute to the Main Peaks of the Nonlinear Infrared Signals

eigenstate	frequency ( $\text{cm}^{-1}$ )	description <sup>a</sup>	contributing basis states
1	0.0	S, ground state	(0), (1 <sub>2</sub> ), (2 <sub>1</sub> ), (2 <sub>2</sub> ), (2 <sub>1</sub> 2 <sub>2</sub> ), (4 <sub>1</sub> ), (2 <sub>1</sub> 2 <sub>2</sub> ), (4 <sub>1</sub> 2 <sub>2</sub> ), ...
2	25.7	A, ground state	-(1 <sub>1</sub> ), -(1 <sub>1</sub> 2 <sub>2</sub> ), -(3 <sub>1</sub> ), -(1 <sub>2</sub> 2 <sub>2</sub> ), -(3 <sub>1</sub> 2 <sub>2</sub> ), -(5 <sub>1</sub> ), ...
22	2339.6	S, O-H/RC1( $v=1$ )	-(0), -(1 <sub>2</sub> ), -(2 <sub>1</sub> ), (1 <sub>1</sub> 2 <sub>1</sub> 3), (3 <sub>1</sub> 1 <sub>3</sub> ), (3 <sub>1</sub> 2 <sub>1</sub> 3), ...
25	2491.8	A, O-H/RC1( $v=1$ )	(1 <sub>1</sub> ), (1 <sub>1</sub> 2 <sub>2</sub> ), -(1 <sub>2</sub> 1 <sub>3</sub> ), -(2 <sub>1</sub> 1 <sub>3</sub> ), -(4 <sub>1</sub> 1 <sub>3</sub> ), -(5 <sub>1</sub> 2 <sub>2</sub> ), ...
80	4004.0	S, O-H/RC1( $v=2$ )	(1 <sub>6</sub> ), -(1 <sub>1</sub> 1 <sub>5</sub> ), -(1 <sub>1</sub> 2 <sub>1</sub> 1 <sub>5</sub> ), (2 <sub>1</sub> 1 <sub>3</sub> 1 <sub>5</sub> ), (4 <sub>1</sub> 1 <sub>3</sub> 1 <sub>5</sub> ), ...
82	4065.4	S, O-H/RC1( $v=1$ )C=O( $v=1$ )	-(1 <sub>6</sub> ), -(1 <sub>1</sub> 1 <sub>5</sub> ), (2 <sub>2</sub> 1 <sub>3</sub> 1 <sub>5</sub> ), (1 <sub>1</sub> 2 <sub>1</sub> 1 <sub>3</sub> 1 <sub>6</sub> ), (1 <sub>1</sub> 2 <sub>1</sub> 1 <sub>3</sub> 1 <sub>6</sub> ), ...
92	4257.3	A, O-H/RC1( $v=2$ )	-(1 <sub>1</sub> ), -(1 <sub>3</sub> ), (3 <sub>1</sub> ), (1 <sub>1</sub> 2 <sub>3</sub> ), (3 <sub>1</sub> 2 <sub>3</sub> ), (3 <sub>1</sub> 1 <sub>2</sub> 2 <sub>3</sub> ), (5 <sub>1</sub> 2 <sub>3</sub> ), ...
112	4596.6	S, O-H/RC1( $v=2$ )RC2( $v=1$ )	-(5 <sub>1</sub> 1 <sub>2</sub> 1 <sub>3</sub> ), ...
118	4665.8	S, O-H/RC1( $v=2$ )	(1 <sub>2</sub> ), -(1 <sub>1</sub> 1 <sub>3</sub> ), (1 <sub>2</sub> 2 <sub>3</sub> ), (2 <sub>1</sub> 2 <sub>3</sub> ), (2 <sub>1</sub> 1 <sub>2</sub> 2 <sub>3</sub> ), (4 <sub>1</sub> 2 <sub>3</sub> ), (3 <sub>1</sub> 2 <sub>1</sub> 3), ...
134	4836.9	A, O-H/RC1( $v=3$ )	(1 <sub>3</sub> ), (1 <sub>1</sub> 1 <sub>2</sub> 2 <sub>3</sub> ), (1 <sub>1</sub> 2 <sub>2</sub> 2 <sub>3</sub> ), (1 <sub>1</sub> 3 <sub>2</sub> 2 <sub>3</sub> ), -(5 <sub>1</sub> 2 <sub>3</sub> ), -(7 <sub>1</sub> 3 <sub>2</sub> ), ...
245	5939.6	A, O-H/RC1( $v=3$ )C=O( $v=1$ )	(1 <sub>1</sub> 1 <sub>6</sub> ), (1 <sub>3</sub> 1 <sub>6</sub> ), -(3 <sub>1</sub> 2 <sub>3</sub> 1 <sub>6</sub> ), -(3 <sub>1</sub> 1 <sub>2</sub> 2 <sub>3</sub> 1 <sub>6</sub> ), -(5 <sub>1</sub> 2 <sub>3</sub> 1 <sub>6</sub> ), ...

<sup>a</sup> The term ( $v = n$ ) represents  $v$  vibrational quanta on mode  $n$ .

signal. A homogeneous line width of  $10 \text{ cm}^{-1}$  was assumed for all transitions.

The calculated  $\mathbf{k}_I$  signals are displayed in Figure 8. The DW and SW signals have very different cross-peak patterns. The SW signal consists of the diagonal peaks  $(-\omega_1, \omega_3) = (-1743, 1743)$  and  $(-2828, 2828)$  and their cross peaks. This is common for harmonic and moderately anharmonic systems. In general, in moderately anharmonic systems, the sidebands appear near the diagonal peaks, because of the energy difference between the transition from  $v = 0$  to  $v = 1$  and the transition from  $v =$

1 to  $v = 2$  of each mode.<sup>53</sup> However, the DW signal shows several off-diagonal peaks, with no corresponding diagonal peaks, which is very unique to this system.

Figures 9 and 10 show the Liouville space pathways, depicted as double-sided Feynman diagrams that contribute to the main peaks in the  $\mathbf{k}_I$  signal of the DW potential. The corresponding energy-level schemes are shown to the right of the respective diagrams. The frequency and the eigenvector of the vibrational eigenstates involved in the signals of  $\mathbf{k}_I, \dots, \mathbf{k}_{IV}$  direction are given in Table 5. The calculated transition dipole moments that

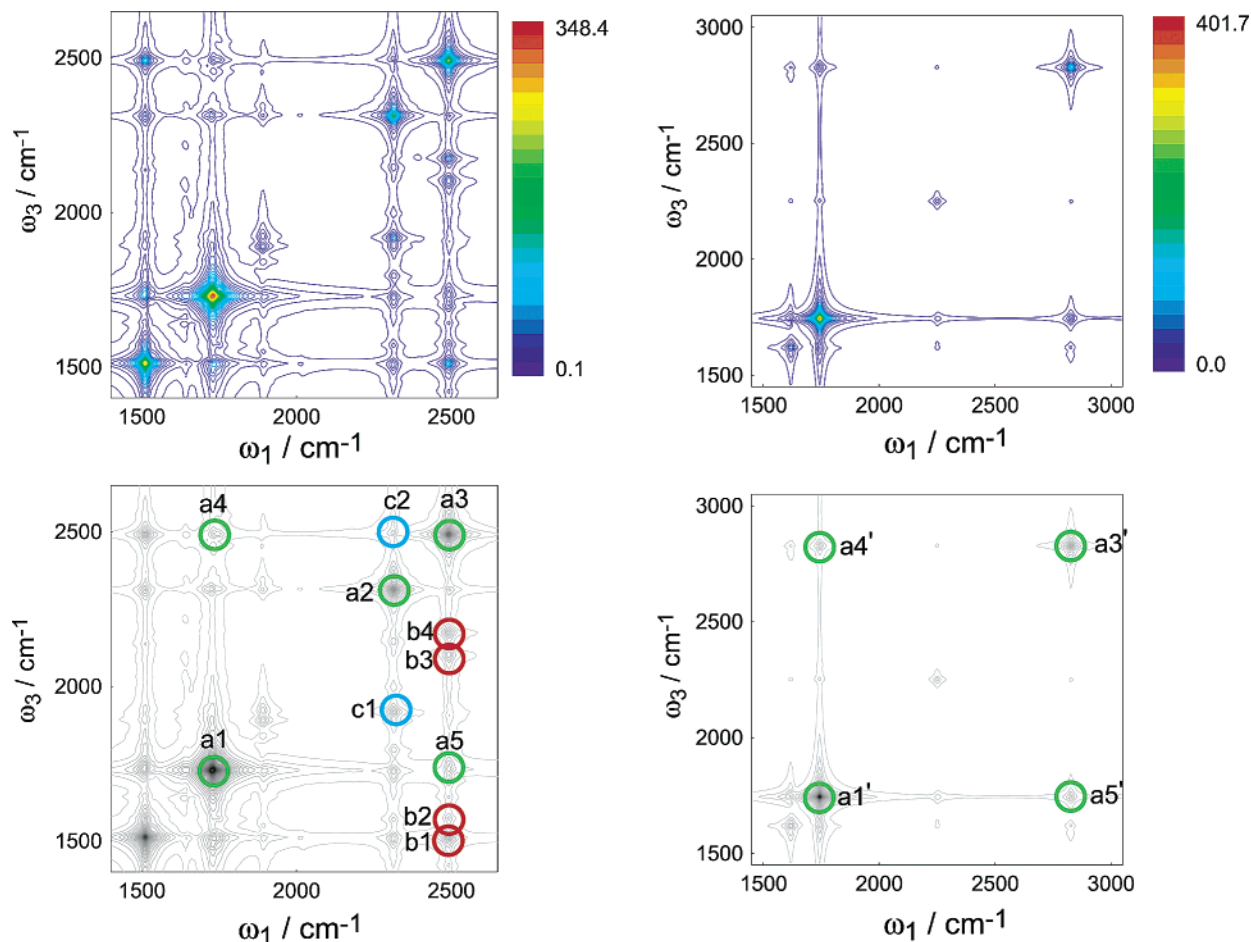


**Figure 11.** Three-pulse  $k_{RR}$  signal ( $S(\omega_1, t_2 = 0, \omega_3)$  in eq 13) of MA. The three incident pulses (10 fs) are tuned to  $2200\text{ cm}^{-1}$  and have a bandwidth of  $\pm 700\text{ cm}^{-1}$  (left) DW model data and (right) SW model data. Top figures are the signals, and bottom figures highlight the main peaks with colored circles and denotations. Peaks with red and blue circles in the DW signal are originating from the Liouville space paths that involve transitions from the A,C=O/RC1( $\nu = 1$ ) and S,C=O/RC1( $\nu = 1$ ) states to higher excited states, respectively. Remaining peaks are marked with green circles. The Liouville space paths of the peaks are shown in Figures 12 and 13.

are responsible for the major features in these signals are displayed in Table 6.

Figure 9 shows that the two strong diagonal a1 and a3 peaks, located at  $(-\omega_1, \omega_3) = (-1732, 1732)$  and  $(-2491, 2491)$  in Figure 8, correspond to the transition between the ground state and state 13 (S,C=O( $\nu = 1$ )) and state 25 (A,O-H/RC1( $\nu = 1$ )), respectively. The intensity is proportional to  $\mu_{1,13}^4$  and  $\mu_{1,25}^4$ . Peaks a4 ( $-1732, 2491$ ) and a5 ( $-2491, 1732$ ) correspond to the diagrams that include the two transitions between the ground state and state 13 (S,C=O( $\nu = 1$ )) and the two transitions between the ground state and state 25 (A,O-H/RC1( $\nu = 1$ )). Therefore, the IR intensity is proportional to  $\mu_{1,13}^2 \mu_{1,25}^2$ . Peak a2 ( $-2314, 2314$ ) comes from the transition between the second ground state (A, ground state) and state 23 (S,O-H( $\nu = 1$ )). Peaks a1' and a3', ..., a5' of the SW signal come from the same pathways as the corresponding peaks in the DW signal.

Other peaks listed in Figure 10 carry information about higher excited states. All off-diagonal peaks (b1, ..., b4) located at  $(\omega_2, -\omega_3) = (-2491, x)$  come from the transition between the ground state and state 25 (A,O-H( $\nu = 1$ )) and the transition from state 25 to higher excited states  $n$  ( $n = 80, 82, 112, 118$ ). States 80 and 82 are mixtures of symmetric O-H/RC1( $\nu = 2$ ) and symmetric O-H/RC1( $\nu = 1$ )C=O( $\nu = 1$ ) that are due to the Fermi resonance. State 112 is symmetric O-H/RC1( $\nu = 2$ )-RC2( $\nu = 1$ ), and state 118 is symmetric O-H/RC1( $\nu = 2'$ ). The term  $2'$  represents the two nodes in a potential minimum, which are different from those of state 82 (S,O-H/RC1( $\nu = 2$ )).

There are three basis states with two quanta in O-H and RC1 modes at one potential minimum (O-H( $\nu = 2$ ), O-H( $\nu = 1$ )-RC( $\nu = 1$ ), RC( $\nu = 2$ )), which results in three eigenstates with two nodes in the O-H/RC1 plane at that geometry. Two of them (states 82 and 118) are optically allowed from state 25 (A,O-H( $\nu = 1$ )). The anharmonic frequency shift ( $\Delta\omega = 2\omega_{S,O-H/RC1(\nu=1)} - \omega_{S,O-H/RC1(\nu=2)}$ ) is  $676\text{ cm}^{-1}$ , which is much larger than that of moderate anharmonic systems ( $5\text{--}29\text{ cm}^{-1}$  in DABCODO<sup>53</sup>). Because of this strong anharmonicity, no diagonal peaks related to these off-diagonal peaks are observed.

Peaks c1 and c2 located at  $(-\omega_2, \omega_3) = (-2314, x)$  come from the transition from the ground state to state 22 (O-H stretch) and the transition from the state 22 to the higher excited states  $n$  ( $n = 92, 134$ ). States 92 and 134 are the second and antisymmetric third overtone of the mixture of O-H stretch and the reaction coordinate, antisymmetric O-H/RC1( $\nu = 2$ ) and antisymmetric O-H/RC1( $\nu = 3$ ). The anharmonic frequency shift ( $\Delta\omega = 2\omega_{A,O-H/RC1(\nu=1)} - \omega_{A,O-H/RC1(\nu=2)}$ ) is also quite large ( $727\text{ cm}^{-1}$ ). The value of the expression  $\Delta\omega = 3\omega_{A,O-H/RC1(\nu=1)} - \omega_{A,O-H/RC1(\nu=3)}$  is  $2639\text{ cm}^{-1}$ . The intense ( $-2314, 4837$ ) peak comes from the allowed transition from antisymmetric O-H/RC1( $\nu = 1$ ) to antisymmetric O-H/RC1( $\nu = 3$ ) and is also attributed to the extraordinarily strong anharmonicity.

**5.2. The  $k_{RR}$  Signal.** The three incident pulses (10 fs) were tuned to  $2200\text{ cm}^{-1}$  with a rectangular bandwidth of  $\pm 700\text{ cm}^{-1}$ .

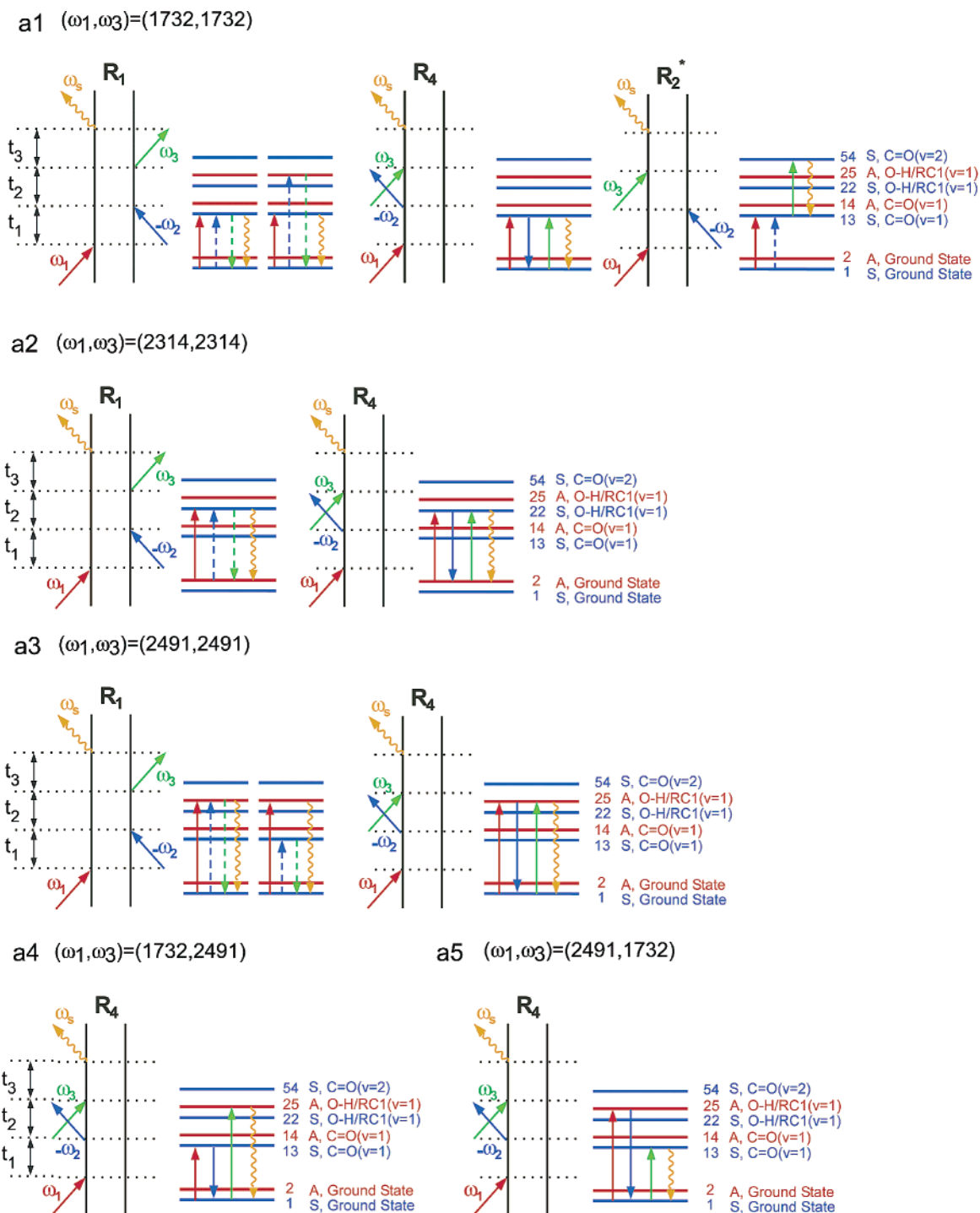


Figure 12. Feynman diagrams and energy-level schemes of the main peaks in the  $k_{II}$  signals of the DW potential. (I)

This resulted in a total of 51 752 terms contributing to the signal.

The calculated  $k_{II}$  signals are displayed in Figure 11. Figures 12 and 13 show the Liouville space pathways that contribute to the main peaks in  $k_{II}$  of the DW potential.

In the DW signal, off-diagonal peaks b1–b4, c1, and c2 involve the same optical transitions as the corresponding peaks in the  $k_I$  signal (see Figure 13), but in a different combination of bra and ket as well as in different time ordering.  $R_1^*$  paths contribute to the off-diagonal peaks in the  $k_I$  signal, but  $R_2^*$  paths are the cause of the off-diagonal peaks in the  $k_{II}$  signal. In  $R_1^*$ , the ket first interacts with  $-\omega_1$ , then the bra interacts with  $\omega_2$  and  $\omega_3$ . In  $R_2^*$ , the bra interacts with  $\omega_1$ ,  $\omega_2$ , and  $-\omega_3$

sequentially, which is directly related to the observed direction ( $k_I = -k_1 + k_2 + k_3$  and  $k_{II} = k_1 + k_2 - k_3$ ).

**5.3. The  $k_{III}$  Signal.** The three incident pulses (10 fs) were tuned to  $2200 \text{ cm}^{-1}$  with a rectangular bandwidth of  $\pm 700 \text{ cm}^{-1}$ . This resulted in a total of 116 706 terms contributing to the signal.

The calculated  $k_{III}$  signals for both the original DW potential and the SW model potential are displayed in Figure 14. Figures 15 and 16 show the Liouville space pathways that contribute to the main peaks in the  $k_{III}$  signal of the DW potential.

In the DW signals, peak b1 (4004, 2491) and b2 (4004, 1512) involve the same optical transitions (two times of the transitions between the S ground state and antisymmetric O–H/RC1( $v =$

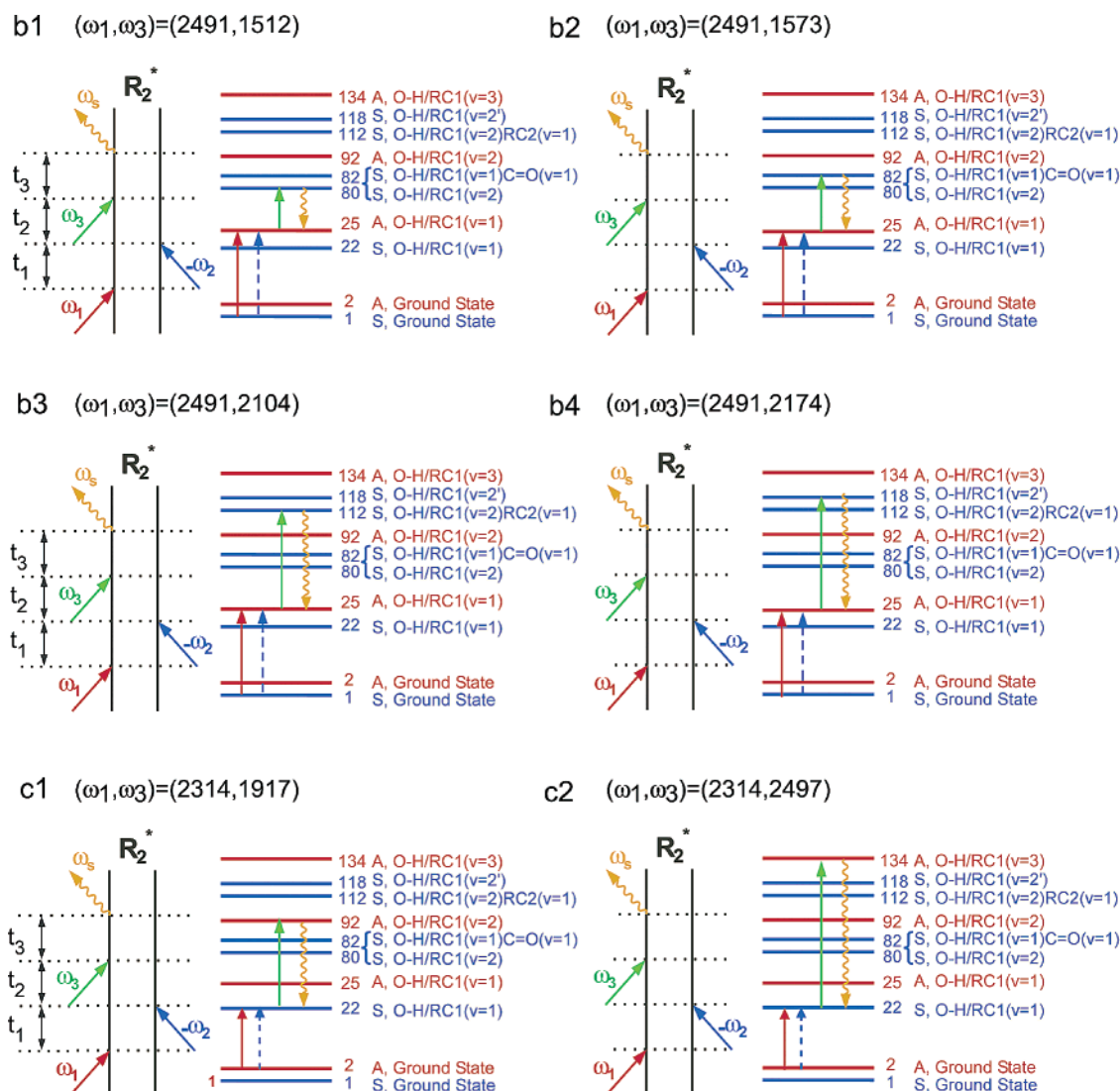


**Figure 13.** Feynman diagrams and energy-level schemes of the main peaks in the  $\mathbf{k}_{II}$  signals of the DW potential. (II)

1) and two times of the transitions between antisymmetric O–H/RC1( $v = 1$ ) and antisymmetric O–H/RC1( $v = 2$ )) but in different time ordering ( $R_4$  and  $R_3^*$ ). Peak pairs of b3 and b4, b5 and b6, b7 and b8, c1 and c2, and c3 and c4 also have the same optical transition in a different combination of bra and ket, as well as in different time ordering. Two pathways,  $R_4$  and  $R_3^*$  that involve the transition between the S ground state and symmetric C=O( $v = 1$ ) and the transition between symmetric C=O( $v = 1$ ) and symmetric C=O( $v = 2$ ) contribute to a degenerate peak a1 at (3465, 1732), because of the harmonicity of the C=O stretch. The b1' peak in the SW signal involves the transitions between O–H( $v = 1$ ) and O–H( $v = 2$ ), which correspond to the b1 peak in the DW signal but is located in a region of much higher frequency. The b3' and b4' peaks in the SW signal also correspond to the b3 and b4 peaks in the DW signal, which involve the transitions between O–H( $v = 1$ ) and O–H( $v = 1$ )C=O( $v = 1$ ). In contrast, the symmetric O–H/RC1( $v = 2$ ) and symmetric O–H/RC1( $v = 1$ )C=O( $v = 1$ ) states of the DW signal are almost degenerate and, in Fermi resonance, O–H( $v = 2$ ) and O–H( $v = 1$ )C=O( $v = 1$ ) of the SW signal are 1076  $\text{cm}^{-1}$  apart.

**5.4. The  $\mathbf{k}_{IV}$  Signal.** The three incident pulses (10 fs) were tuned to 2200, 2200, and 1500  $\text{cm}^{-1}$  with a rectangular bandwidth of  $\pm 700 \text{ cm}^{-1}$ . This tuning resulted in a total of 122 891 pathways being involved in the signal. The calculated

$\mathbf{k}_{IV}$  signals for both the original DW potential and the SW model potential are displayed in Figure 17. Figure 18 shows the Liouville space pathways that correspond to the main peaks in  $\mathbf{k}_{IV}$  of the DW potential.

In Figure 18, the Liouville pathways have different transitions from  $\mathbf{k}_I$  to  $\mathbf{k}_{III}$ . Every pathway involved is the transition to state 245 (A, O–H/RC1( $v = 3$ )C=O( $v = 1$ )). In the SW signal, there are no peaks that involve the transition to O–H( $v > 3$ ), because these states lie above 6000  $\text{cm}^{-1}$  and are not included in our calculations.

To identify the origin of the unusual large anharmonic frequency shift, the vibrational eigenfunctions projected onto the two coordinates  $Q_1$  and  $Q_3$  are plotted in Figure 19. The eigenfunctions of states 1 and 2 have two maxima at the equilibrium geometries G1 and G2. State 1 has the same sign (symmetric), but state 2 has an opposite sign (antisymmetric). The eigenfunctions other than the split ground states are complicated and different from the eigenfunctions that are expected for harmonic systems. There are no clearly defined nodes that can be assigned to each coordinate. Therefore, our study was based on the total number of nodes in the plane at each potential minimum. The strongly distorted shape of the eigenfunctions could be the primary cause of the exceptionally large anharmonic shift. States 92 and 134 are antisymmetric and optically allowed from state 22. The eigenfunction of state

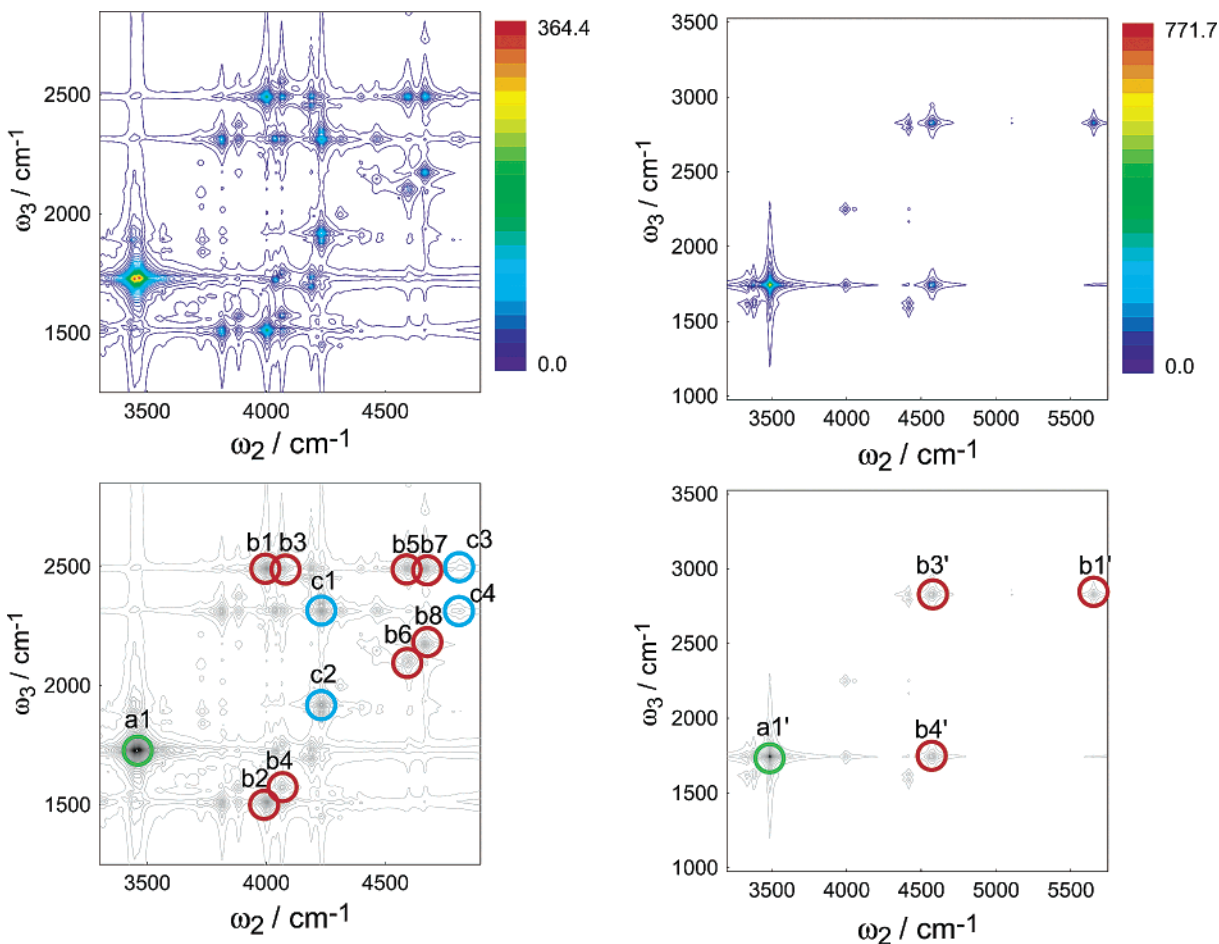


**Figure 14.** Three-pulse  $k_{III}$  signal ( $S(t_1 = 0, \omega_2, \omega_3)$  in eq 14) of malonaldehyde (MA). The three incident pulses (10 fs) are tuned to  $2200\text{ cm}^{-1}$  and have a bandwidth of  $\pm 700\text{ cm}^{-1}$  (left) DW model data and (right) SW model data. Top figures are the signals, and bottom figures highlight the main peaks with colored circles and denotations. Peaks with red and blue circles in the DW signal are coming from the Liouville space paths that involve transitions from the A,C=O/RC1( $v = 1$ ) and S,C=O/RC1( $v = 1$ ) states to higher excited states, respectively. Remaining peaks are marked with green circles. Liouville space paths of the peaks are shown in Figures 15 and 16.

**TABLE 6: Transition Dipole Moments Responsible for Major Features in Two-Dimensional Infrared Spectra<sup>a</sup>**

states		transition dipole moment (normalized to $ \mu_{1,25} $ )			
$a$	$b$	$(\mu_{ab})_x$	$(\mu_{ab})_y$	$(\mu_{ab})_z$	$ \mu_{ab} $
1	13	0.000	0.000	-0.985	0.985
1	25	0.000	1.000	0.000	1.000
1	92	0.000	0.075	0.000	0.075
2	22	0.000	0.927	0.000	0.927
13	54	0.000	0.000	1.321	1.321
22	25	0.000	0.927	0.000	0.927
22	80	0.000	0.000	-0.594	0.594
22	82	0.000	0.000	0.829	0.829
22	92	0.000	-1.135	0.000	1.135
22	134	0.000	-0.444	0.000	0.444
25	80	0.000	-0.617	0.000	0.617
25	82	0.000	-0.549	0.000	0.549
25	92	0.000	0.000	0.071	0.071
25	112	0.000	-0.768	0.000	0.768
25	118	0.000	0.966	0.000	0.966
80	92	0.000	-0.290	0.000	0.290
80	245	0.000	-1.369	0.000	1.369
82	92	0.000	0.200	0.000	0.200
82	245	0.000	1.123	0.000	1.123
92	112	0.000	0.322	0.000	0.322
92	118	0.000	-0.744	0.000	0.744
92	245	0.000	0.000	-1.697	1.697
112	134	0.000	0.251	0.000	0.251
118	134	0.000	0.422	0.000	0.422
118	245	0.000	0.182	0.000	0.182

<sup>a</sup> The  $x$ -,  $y$ -, and  $z$ -axes are defined in Figure 2.

92 has two nodes in each equilibrium geometry. Therefore, this state is the second excited state of O–H stretch. The eigenfunction of state 134 has three nodes in each equilibrium geometry, and, thus, this state is the third excited state of the O–H stretch mode. Therefore, the peaks at (2314, -1917) and (2314, -2497) respectively represent the second and third harmonics of the O–H stretch mode. States 80, 82, 112, and 118 are all symmetric and optically allowed from state 25. States 80 and 82 are the mixed states obtained from the second harmonics of the O–H stretch mode and the combination band of the O–H stretch and the C=O stretch with the Fermi resonance. State 112 is the combination band of C=O/RC1( $v = 2$ ) and RC2( $v = 1$ ). State 118 also has two nodes in each potential minimum.

## 6. Discussion

We have conducted an ab initio simulation of three pulse nonlinear IR signals of an intramolecular hydrogen-bonded system. The signals were calculated using a six-coordinate DW vibrational potential of MA. To pinpoint the effect of proton transfer on the 2-D peak pattern, the signals calculated for the DW potential are compared with those of the SW model potential, where proton transfer is prohibited. We found some clear signatures of intramolecular proton transfer. Several new off-diagonal peaks in the signals of the DW potential, which are absent in the SW signals, are clear markers for the proton

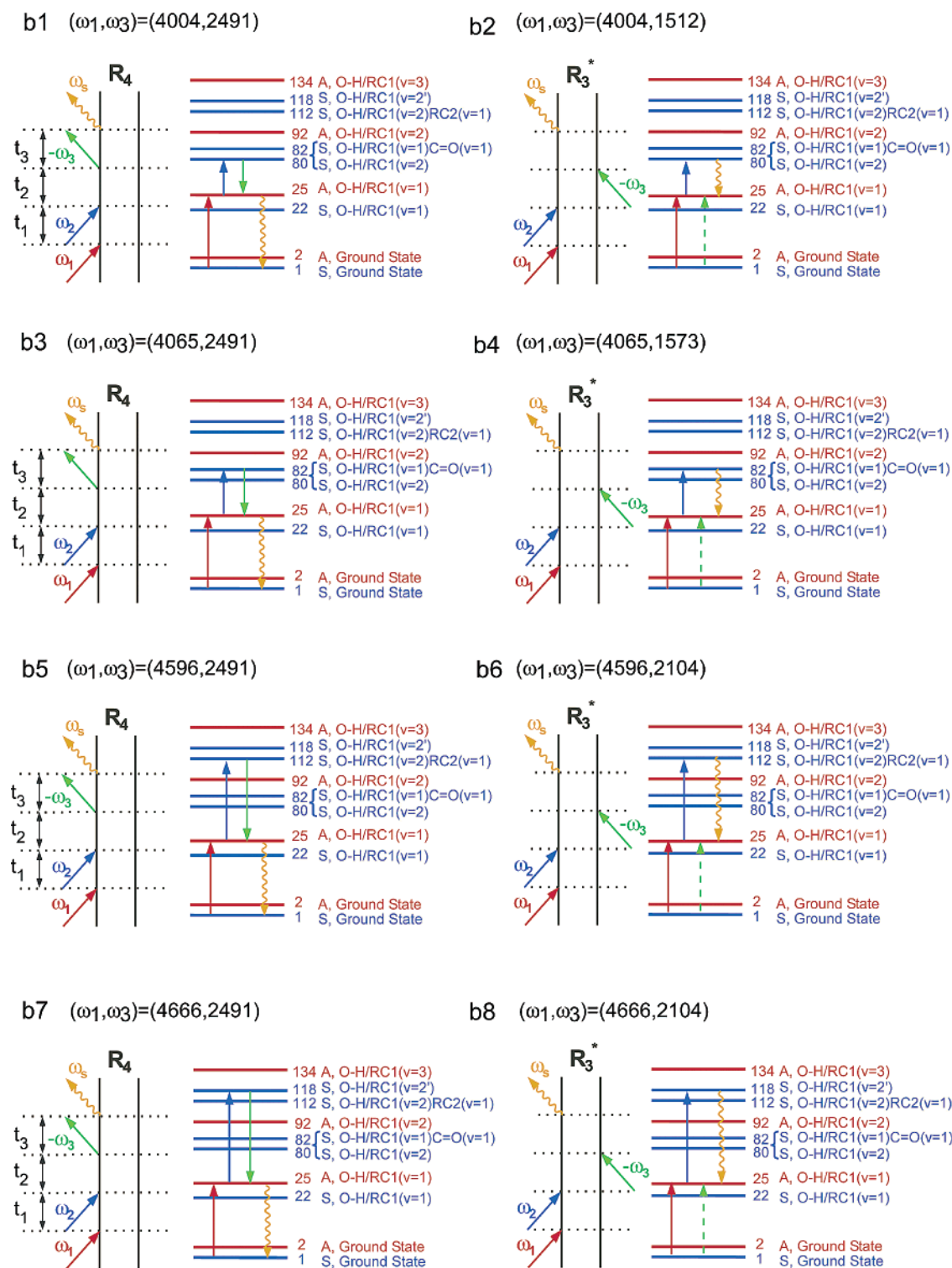


**Figure 15.** Feynman diagrams and energy-level schemes of the main peaks in the  $k_{III}$  signals of the DW potential. (I)

transfer. Many signatures of proton transfer in experimental linear spectra are hidden under a large broadening envelope where the peak shift of the O–H stretch is noticeable. However, in 2-D signals, the new peaks due to proton transfer should be resolved, even in solution. The IR peak positions are very sensitive to the PES along the transfer coordinates and to the solvent environment. Therefore, nonlinear IR signals could be useful for investigating proton transfer and its coupling to the solvent dynamics.

The proton-transfer reaction path has been described<sup>14</sup> by the path in the 2-D configuration space spanned by two basis

vectors; one connects the two minima in the shortest path, the other connects the transition state and the midpoint of two minima. Therefore, we constructed the six coordinates that were generated from these two reaction basis vectors and four other vectors that correspond to the C=O stretch and O–H stretch normal modes at G1 and G2 local minima, using Gram–Schmidt orthogonalization. The MP2 level predicts the proton-transfer barrier that is the most similar to that of the experiment, and we have adopted this level of theory to calculate an anharmonic force field for these six coordinates. A sixth-order force field was necessary to reach convergence of the numerical

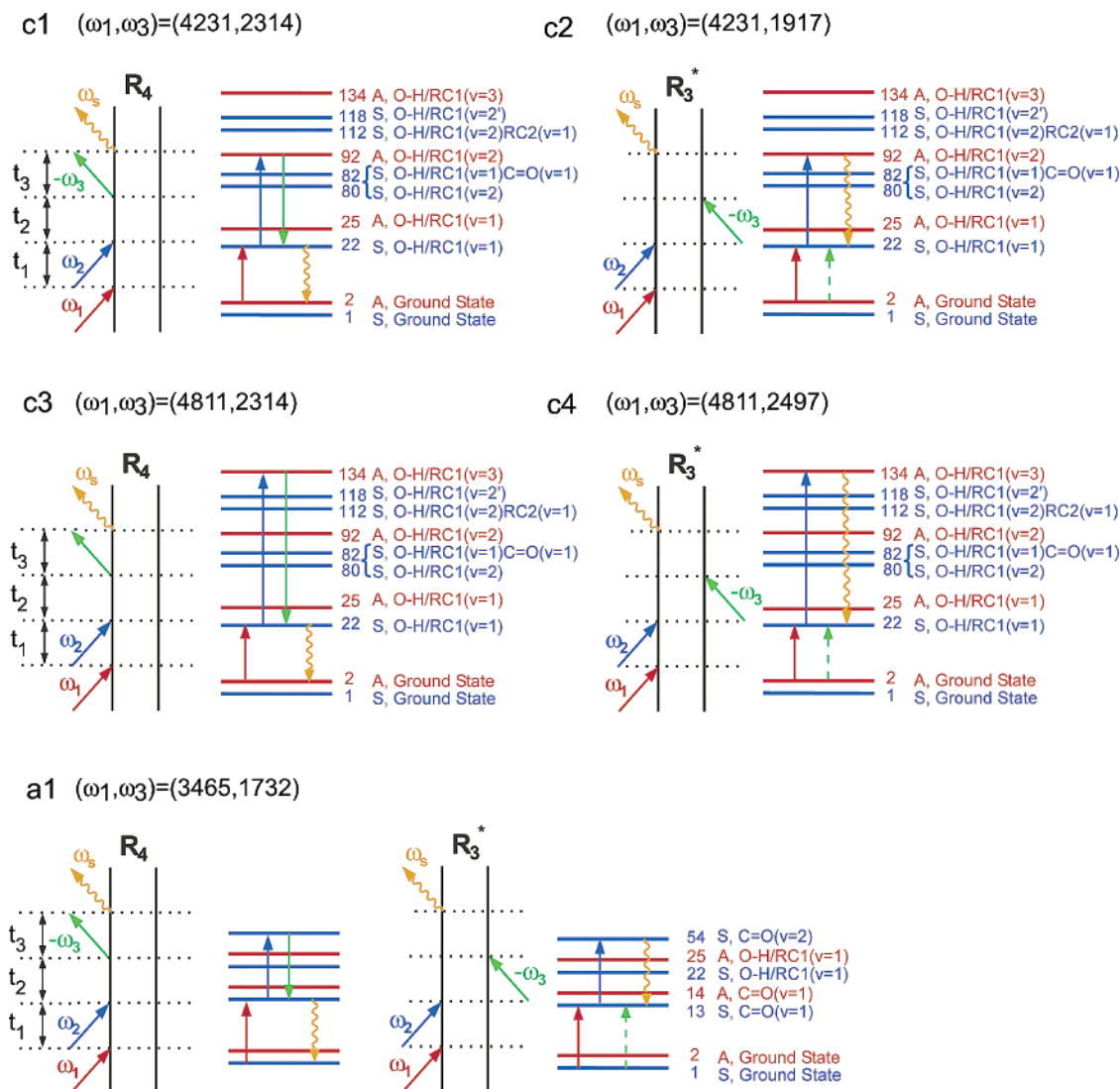


**Figure 16.** Feynman diagrams and energy-level schemes of the main peaks in the  $k_{III}$  signals of the DW potential. (II)

differentiation and is used in our calculations, even though quartic force fields were used in previous studies of proton-transfer systems.<sup>24,25</sup>

To compute the eigenstates of the DW anharmonic Hamiltonian, we used a harmonic oscillator basis set with arbitrary frequencies and center positions. We calculated the eigenstates and energies, keeping 36 total excitations among these six coordinates, which resulted in 73 728 states (DW). IRAM was used to solve this large-scale eigenvalue problem. A total of 245 states (DW) lie below 6000  $\text{cm}^{-1}$ , which is the frequency range covered by the spectroscopic techniques that are presented here. The tunneling splitting of the ground state was 25.6  $\text{cm}^{-1}$ , which was in good agreement with the experimental value (21.6  $\text{cm}^{-1}$ ).

Three pulse nonlinear IR signals for the DW and SW potentials along the four phase-matching directions were simulated. In all cases, we found new off-diagonal peaks in the DW potential that are absent in the SW potential and may be attributed to the strong anharmonic coupling between the O–H stretch and the two reaction coordinates. The transition between antisymmetric O–H/RC1( $v=1$ ) and symmetric O–H/RC1( $v=2$ ) and the transition between symmetric O–H/RC1( $v=1$ ) and antisymmetric O–H/RC1( $v=2$ ) and antisymmetric O–H/RC1( $v=3$ ) contributed to these peaks, and the transition frequencies have a much lower frequency than the fundamental

frequency. This unusually large anharmonic frequency shift may be attributed to the very strong coupling between  $Q_1$  and  $Q_3$  and the highly distorted wave functions that are plotted in Figure 19.

The highly excited vibrational eigenstates in the region of 4000–5000  $\text{cm}^{-1}$ , which may be reached by the transition from the O–H fundamental, are delocalized along the reaction plane and, therefore, are very sensitive to the PES along the proton-transfer coordinates. Three pulse nonlinear IR spectroscopy shows the peaks obtained from such transitions simultaneously. The spectra change quantitatively with the different levels of ab initio calculation or by the selection of different coordinates.

The inclusion of additional coordinates may be the next step to improve the modeling of proton-transfer systems.<sup>56</sup> However, the required numerical effort rapidly grows with the number of coordinates. The dynamics of MA in solution is another possible focus of future study. In that case, solvent dynamics can be treated classically, and the Coulombic interaction between MA and solvent may be included to calculate the vibrational eigenstate of MA. The present approach is directly applicable to other DW hydrogen-bonded systems, such as DNA base pairs<sup>54</sup> and peptides<sup>55</sup> with hydrogen bondings.

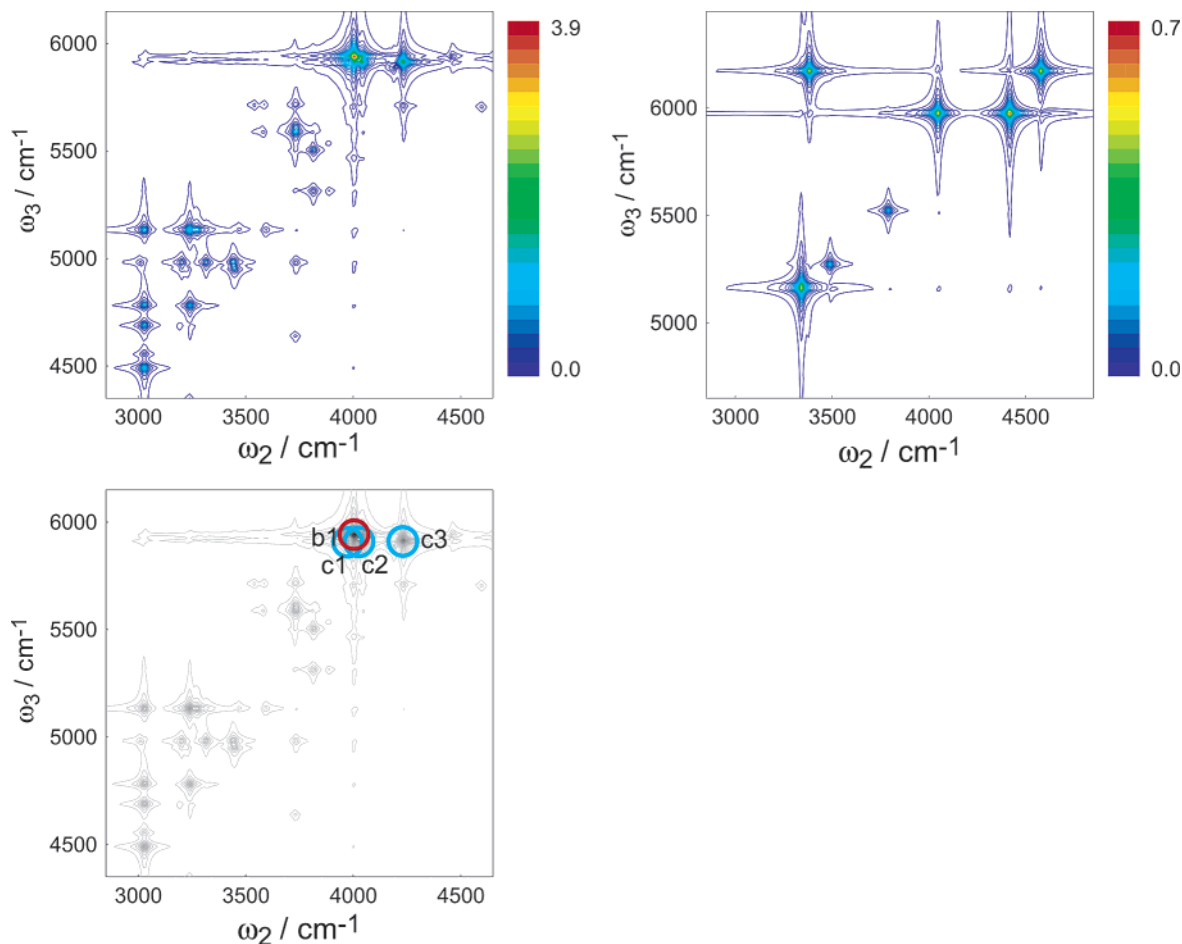


**Figure 17.** Three-pulse  $\mathbf{k}_{IV}$  signal ( $S(t_1 = 0, \omega_2, \omega_3)$  in eq 14) of malonaldehyde (MA). The three incident pulses (10 fs) are tuned to 2200, 2200, and 1500  $\text{cm}^{-1}$  and have a bandwidth of  $\pm 700 \text{ cm}^{-1}$  (left) DW model data and (right) SW model data). Top figures are the signals, and bottom figure highlights the main peaks with colored circles and denotations. Peaks with red and blue circles are originating from the Liouville space paths that involve transitions from A,C=O/RC1( $\nu = 1$ ) and S,C=O/RC1( $\nu = 1$ ) state to higher excited states, respectively. The Liouville space paths of the peaks are shown in Figure 18.

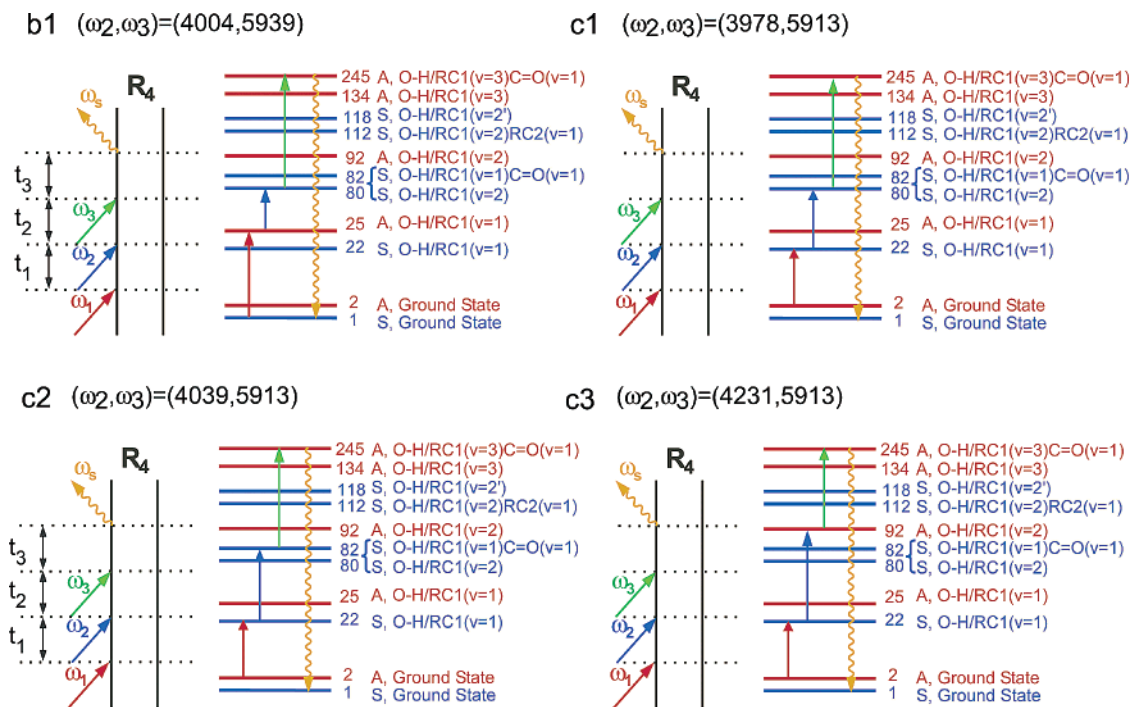


**Figure 18.** Feynman diagrams and energy-level schemes of the main peaks in the  $\mathbf{k}_{IV}$  signals of the DW potential.

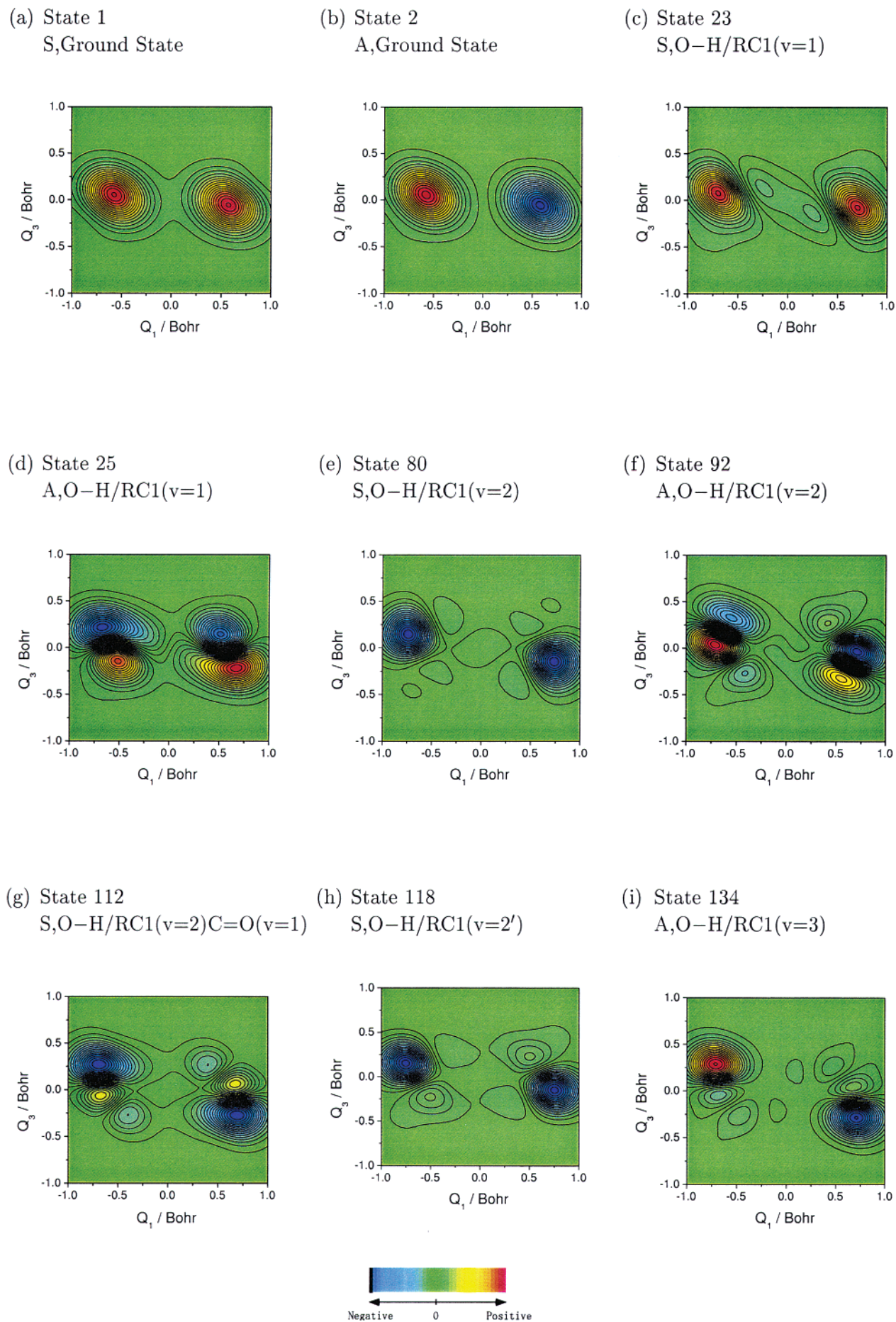


Figure 19. Vibrational eigenfunctions of the DW potential projected to the two reaction coordinates  $Q_1$  and  $Q_3$ .

**Appendix A: Gram–Schmidt Orthogonalization**

Normalizations and Gram–Schmidt orthogonalizations<sup>46</sup> of the six basis vectors  $\xi'_1, \dots, \xi'_6$  were performed in the following order:

$$\xi_1 \equiv \frac{\xi'_1}{\|\xi'_1\|} \quad (\text{A1})$$

$$\xi_2 \equiv \frac{\xi'_2}{\|\xi'_2\|} \quad (\text{A2})$$

$$\xi_3 \equiv \frac{\xi'_3 - (\xi'_3 \cdot \xi_1)\xi_1}{\|\xi'_3 - (\xi'_3 \cdot \xi_1)\xi_1\|} \quad (\text{A3})$$

$$\xi_4 \equiv \frac{\xi'_4 - (\xi'_4 \cdot \xi_2)\xi_2}{\|\xi'_4 - (\xi'_4 \cdot \xi_2)\xi_2\|} \quad (\text{A4})$$

$$\xi_5 \equiv \frac{\xi'_5 - (\xi'_5 \cdot \xi_1)\xi_1 - (\xi'_5 \cdot \xi_3)\xi_3}{\|\xi'_5 - (\xi'_5 \cdot \xi_1)\xi_1 - (\xi'_5 \cdot \xi_3)\xi_3\|} \quad (\text{A5})$$

$$\xi_6 \equiv \frac{\xi'_6 - (\xi'_6 \cdot \xi_2)\xi_2 - (\xi'_6 \cdot \xi_4)\xi_4}{\|\xi'_6 - (\xi'_6 \cdot \xi_2)\xi_2 - (\xi'_6 \cdot \xi_4)\xi_4\|} \quad (\text{A6})$$

where  $\xi'_1, \xi'_3$ , and  $\xi'_5$  have  $B_2$  symmetry, and  $\xi'_2, \xi'_4$ , and  $\xi'_6$  have  $A_1$  symmetry. The vectors in a different symmetry do not mix with each other in this orthogonalization.

**Appendix B: Numerical Differentiations**

We calculated the five-point central difference formulas in the same way as the three-point formulas given in ref 47 to obtain the anharmonic force constants  $f_{ij}^{(3)}$  to  $f_{ij1111}^{(6)}$ . Third-order to sixth-order derivatives ( $f_{ijk}^{(3)}, f_{ijkk}^{(4)}, f_{ijkkk}^{(5)}$ , and  $f_{ijkkkk}^{(6)}$ ) are calculated from the numerical differentiation of the quadratic derivatives ( $f_{ij}^{(2)}$ ), with respect to the single coordinate  $Q_k$ , as

$$f_{ijk}^{(3)} = \frac{\delta_1^2 \delta_2^2}{\delta_2^2 - \delta_1^2} \left( \frac{f_{ij}^{(2)}(\delta_1) - f_{ij}^{(2)}(-\delta_1)}{2\delta_1^3} - \frac{f_{ij}^{(2)}(\delta_2) - f_{ij}^{(2)}(-\delta_2)}{2\delta_2^3} \right) \quad (\text{B1})$$

$$f_{ijkk}^{(4)} = \frac{\delta_1^2 \delta_2^2}{\delta_2^2 - \delta_1^2} \left( \frac{f_{ij}^{(2)}(\delta_1) + f_{ij}^{(2)}(-\delta_1) - 2f_{ij}^{(2)}(0)}{2\delta_1^4} - \frac{f_{ij}^{(2)}(\delta_2) + f_{ij}^{(2)}(-\delta_2) - 2f_{ij}^{(2)}(0)}{2\delta_2^4} \right) \quad (\text{B2})$$

$$f_{ijkkk}^{(5)} = \frac{1}{\delta_1^2 - \delta_2^2} \left( \frac{f_{ij}^{(2)}(\delta_1) - f_{ij}^{(2)}(-\delta_1)}{2\delta_1} - \frac{f_{ij}^{(2)}(\delta_2) - f_{ij}^{(2)}(-\delta_2)}{2\delta_2} \right) \quad (\text{B3})$$

$$f_{ijkkkk}^{(6)} = \frac{1}{\delta_1^2 - \delta_2^2} \left( \frac{f_{ij}^{(2)}(\delta_1) + f_{ij}^{(2)}(-\delta_1) - 2f_{ij}^{(2)}(0)}{2\delta_1^2} - \frac{f_{ij}^{(2)}(\delta_2) + f_{ij}^{(2)}(-\delta_2) - 2f_{ij}^{(2)}(0)}{2\delta_2^2} \right) \quad (\text{B4})$$

where  $\delta_1$  and  $\delta_2$  are the two displacement steps of  $Q_k$ .

**Appendix C: Excitonic Vibrational Hamiltonian**

The vibrational Hamiltonian was recast in a normally ordered field operator form<sup>36</sup> to sixth order. In ref 36, the frequency and center position of the harmonic oscillator basis set was fixed, and the Hamiltonian was expanded to fourth order. In this study, these formulas are extended to adopt any harmonic oscillator basis set with arbitrarily chosen frequencies and center positions. The diagonal matrix elements of the quadratic field-operator portion associated with  $\omega_i$  and  $U_{ii}^{(2)}$  contain the  $B_i^+ B_i^+$  and  $B_i B_i$  field-operator terms, which will vanish in the limit where the frequency of the basis set for the  $i$ th degree of freedom is equal to that of the potential  $(m_i \omega_i^2/2)/\sqrt{(2m_i \omega_i/\hbar)^2} = U_{ii}^{(2)}$ . The fifth- and sixth-order derivatives are also included in the lower field-operator terms. The Hamiltonian is given by

$$\begin{aligned} \mathcal{H} = & \sum_{i=1}^6 (U_i^{(1)} + 3 \sum_{j=1}^6 U_{ij}^{(3)} + 15 \sum_{j,k=1}^6 U_{ijk}^{(5)}) (B_i^+ + B_i) \\ & + \sum_{ij=1}^6 (U_{ij}^{(2)} + 6 \sum_{k=1}^6 U_{ijk}^{(4)} + 45 \sum_{k,l=1}^6 U_{ijkl}^{(6)}) (2B_i^+ B_j + B_i^+ B_j^+ \\ & + B_i B_j) + \delta_{ij} \frac{m_i \omega_i^2/2}{\sqrt{(2m_i \omega_i/\hbar)^2}} (2B_i^+ B_i - B_i^+ B_i^+ - B_i B_i) \\ & + \sum_{i,j,k=1}^6 (U_{ijk}^{(3)} + 10 \sum_{l=1}^6 U_{ijkl}^{(5)}) (B_i^+ B_j^+ B_k^+ + 3B_i^+ B_j^+ B_k \\ & + 3B_i^+ B_j B_k + B_i B_j B_k) \\ & + \sum_{i,j,k,l=1}^6 (U_{ijkl}^{(4)} + 15 \sum_{m=1}^6 U_{ijklm}^{(6)}) (B_i^+ B_j^+ B_k^+ B_l^+ \\ & + 4B_i^+ B_j^+ B_k^+ B_l + 6B_i^+ B_j^+ B_k B_l \\ & + 4B_i^+ B_j B_k B_l + B_i B_j B_k B_l) \\ & + \sum_{i,j,k,l,m=1}^6 U_{ijklm}^{(5)} (B_i^+ B_j^+ B_k^+ B_l^+ B_m^+ + 5B_i^+ B_j^+ B_k^+ B_l^+ B_m \\ & + 10B_i^+ B_j^+ B_k^+ B_l B_m + 10B_i^+ B_j^+ B_k B_l B_m \\ & + 5B_i^+ B_j B_k B_l B_m + B_i B_j B_k B_l B_m) \\ & + \sum_{i,j,k,l,m,n=1}^6 U_{ijklmn}^{(6)} (B_i^+ B_j^+ B_k^+ B_l^+ B_m^+ B_n^+ \\ & + 6B_i^+ B_j^+ B_k^+ B_l^+ B_m^+ B_n + 15B_i^+ B_j^+ B_k^+ B_l^+ B_m B_n \\ & + 20B_i^+ B_j^+ B_k^+ B_l B_m B_n + 15B_i^+ B_j^+ B_k B_l B_m B_n \\ & + 6B_i^+ B_j B_k B_l B_m B_n + B_i B_j B_k B_l B_m B_n) \end{aligned} \quad (\text{C1})$$

where

$$U_{i_1 i_2 \dots i_n}^{(n)} \equiv \frac{f_{i_1 i_2 \dots i_n}^{(n)'}}{\sqrt{(2m_{i_1} \omega_{i_1}/\hbar)(2m_{i_2} \omega_{i_2}/\hbar) \dots (2m_{i_n} \omega_{i_n}/\hbar)}} \quad (\text{C2})$$

The terms  $f_i^{(1)'}$ ,  $f_{ij}^{(2)'}$ ,  $f_{ijk}^{(3)'}$ ,  $f_{ijkl}^{(4)'}$ ,  $f_{ijkl}^{(5)'}$ , and  $f_{ijkl}^{(6)'}$  are defined as follows:

$$f_i^{(1)'} \equiv f_i^{(1)} - 2 \sum_j f_{ij}^{(2)} A_j + 3 \sum_{j,k} f_{ijk}^{(3)} A_j A_k - 4 \sum_{j,k,l} f_{ijkl}^{(4)} A_j A_k A_l + 5 \sum_{j,k,l,m} f_{ijklm}^{(5)} A_j A_k A_l A_m - 6 \sum_{j,k,l,m,n} f_{ijklmn}^{(6)} A_j A_k A_l A_m A_n \quad (\text{C3})$$

$$f_{ij}^{(2)'} \equiv f_{ij}^{(2)} - 3 \sum_k f_{ijk}^{(3)} A_k + 6 \sum_{k,l} f_{ijkl}^{(4)} A_k A_l - 10 \sum_{k,l,m} f_{ijklm}^{(5)} A_k A_l A_m + 15 \sum_{k,l,m,n} f_{ijklmn}^{(6)} A_k A_l A_m A_n \quad (\text{C4})$$

$$f_{ijk}^{(3)'} \equiv f_{ijk}^{(3)} - 4 \sum_l f_{ijkl}^{(4)} A_l + 10 \sum_{l,m} f_{ijklm}^{(5)} A_l A_m - 20 \sum_{l,m,n} f_{ijklmn}^{(6)} A_l A_m A_n \quad (\text{C5})$$

$$f_{ijkl}^{(4)'} \equiv f_{ijkl}^{(4)} - 5 \sum_m f_{ijklm}^{(5)} A_m + 15 \sum_{m,n} f_{ijklmn}^{(6)} A_m A_n \quad (\text{C6})$$

$$f_{ijkl}^{(5)'} \equiv f_{ijkl}^{(5)} - 6 \sum_n f_{ijklmn}^{(6)} A_n \quad (\text{C7})$$

$$f_{ijkl}^{(6)'} = f_{ijkl}^{(6)} \quad (\text{C8})$$

**Acknowledgment.** We wish to thank Dr. Jens Dreyer and Dr. Andrew Moran for most useful discussions. The support of the National Institutes of Health (under Grant No. RO1 GM59230-01A2) is gratefully acknowledged. This material is based upon work supported by the National Science Foundation, under Grant No. CHE-0132571.

## References and Notes

- (1) Elsaesser, T.; Bakker, H. J., Eds. *Ultrafast Hydrogen Bonding Dynamics and Proton-Transfer Processes in the Condensed Phase*; Kluwer Academic Publishers: Dordrecht, The Netherlands, 2002.
- (2) Zundel, G. *Adv. Chem. Phys.* **2000**, *111*, 1.
- (3) Rowe, W. F.; Duerst, R. W.; Wilson, E. B. *J. Am. Chem. Soc.* **1977**, *99*, 7072.
- (4) Baughcum, S. L.; Duerst, R. W.; Rowe, W. F.; Smith, Z.; Wilson, E. B. *J. Am. Chem. Soc.* **1981**, *103*, 6296.
- (5) Baba, T.; Tanaka, T.; Morino, I.; Yamada, M. T.; Tanaka, K. *J. Chem. Phys.* **1999**, *10*, 4131.
- (6) Firth, D. W.; Beyer, K.; Dvorak, M. A.; Grushow, A.; Loepold, K. R. *J. Chem. Phys.* **1991**, *94*, 1812.
- (7) Baughcum, S. L.; Smith, Z.; Wilson, E. B.; Duerst, R. W. *J. Am. Chem. Soc.* **1984**, *106*, 2260.
- (8) Brown, R. S.; Tse, A.; Nakashima, T.; Hadson, R. C. *J. Am. Chem. Soc.* **1979**, *101*, 3157.
- (9) Seliskar, C. J.; Hoffmann, R. E. *J. Mol. Spectrosc.* **1982**, *96*, 146.
- (10) Schiering, D. W.; Katon, J. E. *Appl. Spectrosc.* **1986**, *40*, 1049.
- (11) Chiavassa, T.; Roubin, P.; Pizzala, L.; Verlaque, P.; Allouche, A.; Marinelli, F. *J. Phys. Chem.* **1992**, *96*, 10659.
- (12) Iftimie, R.; Schofield, J. *J. Chem. Phys.* **2001**, *115*, 5891.
- (13) Gonzalez, C.; Schlegel, H. B. *J. Chem. Phys.* **1989**, *90*, 2154.
- (14) Yagi, K.; Taketsugu, T.; Hirao, K. *J. Chem. Phys.* **2001**, *115*, 10647.
- (15) Polyansky, O. L.; Jensen, P.; Tennyson, J. *J. Chem. Phys.* **1996**, *105*, 6490.
- (16) Lawrence, C. P.; Skinner, J. L. *J. Chem. Phys.* **2002**, *117*, 5827.
- (17) Lawrence, C. P.; Skinner, J. L. *J. Chem. Phys.* **2002**, *117*, 8847.
- (18) Lawrence, C. P.; Skinner, J. L. *J. Chem. Phys.* **2003**, *118*, 264.
- (19) Laenen, R.; Rauscher, C.; Laubereau, A. *J. Phys. Chem. B* **1998**, *102*, 9304.
- (20) Stenger, J.; Madsen, D.; Hamm, P.; Nibbering, E. T. J.; Elsaesser, T. *Phys. Rev. Lett.* **2001**, *87*, 27401.
- (21) Stenger, J.; Madsen, D.; Hamm, P.; Nibbering, E. T. J.; Elsaesser, T. *J. Phys. Chem. A* **2002**, *106*, 2341.

- (22) Woutersen, S.; Emmerichs, U.; Nienhuys, H.-K.; Bakker, H. J. *Phys. Rev. Lett.* **1998**, *81*, 1106.
- (23) Nienhuys, H.-K.; Woutersen, S.; van Santen, R. A.; Bakker, H. J. *J. Chem. Phys.* **1999**, *111*, 1494.
- (24) Benderskii, V. A.; Vetoshkin, E. V.; Irgibaeva, I. S.; Trommsdorff, H.-P. *Russ. Chem. Bull.* **2001**, *50*, 1148.
- (25) Takada, S.; Nakamura, H. *J. Chem. Phys.* **1995**, *102*, 3977.
- (26) Makri, N.; Miller, W. H. *J. Chem. Phys.* **1989**, *91*, 4026.
- (27) Chaban, G. M.; Jung, J. O.; Gerber, R. B. *J. Chem. Phys.* **1999**, *111*, 1823. Gerber, R. B.; Brauer, B.; Gregurick, S. K.; Chaban, G. M. *PhysChemComm* **2002**, *5*, 142. Gerber, R. B.; Chaban, G. M.; Gregurick, S. K.; Brauer, B. *Biopolymers* **2003**, *68*, 370.
- (28) Gregurick, S. K.; Chabin, G. M.; Gerber, R. B. *J. Phys. Chem. A* **2002**, *106*, 8696.
- (29) Harris, D. O.; Engerholm, G. G.; Gwinm, G. W. *J. Chem. Phys.* **1965**, *43*, 1515.
- (30) Light, J. C.; Hamilton, I. P.; Lill, J. V. *J. Chem. Phys.* **1985**, *82*, 1400.
- (31) Meyer, H.-D.; Manthe, U.; Cederbaum, L. S. *Chem. Phys. Lett.* **1990**, *165*, 73.
- (32) Manthe, U.; Meyer, H.-D.; Cederbaum, L. S. *J. Chem. Phys.* **1992**, *97*, 3199.
- (33) Beck, M. H.; Jackle, J.; Worth, G. A.; Meyer, H.-D. *Phys. Rep.* **2000**, *324*, 1.
- (34) Naundorf, H.; Worth, G. A.; Meyer, H.-D.; Kuhn, O. *J. Phys. Chem. A* **2002**, *106*, 719.
- (35) Naundorf, H.; Kuhn, O. *Femtochemistry and Femtobiology*; World Scientific: New Jersey, 2001.
- (36) Moran, A. M.; Park, S.-M.; Dreyer, J.; Mukamel, S. *J. Chem. Phys.* **2003**, *118*, 3651.
- (37) Mukamel, S.; Hochstrasser, R. M., Eds. *Chem. Phys.* **2001**, *266*, (Special issue, Multidimensional Spectroscopies.)
- (38) Mukamel, S. *Annu. Rev. Phys.* **2000**, *51*, 691.
- (39) Demirdoven, N.; Khalil, M.; Golonzka, O.; Tokmakoff, A. *J. Phys. Chem. A* **2001**, *105*, 8025.
- (40) Golonzka, O.; Khalil, M.; Demirdoven, N.; Tokmakoff, A. *J. Chem. Phys.* **2001**, *115*, 10814.
- (41) Rector, K. D.; Zimdars, D.; Fayer, M. D. *J. Chem. Phys.* **1998**, *109*, 5455.
- (42) Wright, J. C.; Chen, P. C.; Hamilton, J. P.; Zilian, A.; Labuda, M. *J. Appl. Spectrosc.* **1997**, *51*, 949.
- (43) Frisch, M. J.; Trucks, G. W.; Schlegel, H. B.; Scuseria, G. E.; Robb, M. A.; Cheeseman, J. R.; Zakrzewski, V. G.; Montgomery, J. A., Jr.; Stratmann, R. E.; Burant, J. C.; Dapprich, S.; Millam, J. M.; Daniels, A. D.; Kudin, K. N.; Strain, M. C.; Farkas, O.; Tomasi, J.; Barone, V.; Cossi, M.; Cammi, R.; Mennucci, B.; Pomelli, C.; Adamo, C.; Clifford, S.; Ochterski, J.; Petersson, G. A.; Ayala, P. Y.; Cui, Q.; Morokuma, K.; Malick, D. K.; Rabuck, A. D.; Raghavachari, K.; Foresman, J. B.; Cioslowski, J.; Ortiz, J. V.; Stefanov, B. B.; Liu, G.; Liashenko, A.; Piskorz, P.; Komaromi, I.; Gomperts, R.; Martin, R. L.; Fox, D. J.; Keith, T.; Al-Laham, M. A.; Peng, C. Y.; Nanayakkara, A.; Gonzalez, C.; Challacombe, M.; Gill, P. M. W.; Johnson, B. G.; Chen, W.; Wong, M. W.; Andres, J. L.; Head-Gordon, M.; Replogle, E. S.; Pople, J. A. *Gaussian 98*, revision A.11; Gaussian, Inc.: Pittsburgh, PA, 1998.
- (44) Barone, V.; Adamo, C. *J. Chem. Phys.* **1996**, *10*, 11007.
- (45) Spirko, V.; Cejchan, A.; Lutchny, R.; Leszczynski, J. *Chem. Phys. Lett.* **2002**, *355*, 319.
- (46) Arfken, G. B.; Weber, H.-J., Eds. *Mathematical Methods for Physicists*; Harcourt/Academic Press: London, 2000.
- (47) Schleyer, P.; Allinger, N.; Clark, T.; Gasteiger, J.; Kollman, P. A.; Schaefer, H. A., III; Schreiner, P. R., Eds. *Encyclopedia of Computational Chemistry*; Wiley: Chichester, U.K., 1998.
- (48) Lehoucq, R. B. Ph.D. Thesis, Rice University, Houston, TX, 1995.
- (49) Lehoucq, R. B.; Sorensen, D. C.; Yang, C. *ARPACK Users Guide: Solution of Large Scale Eigenvalue Problems with Implicitly Restarted Arnoldi Methods*; Society for Industrial and Applied Mathematics: Philadelphia, 1998.
- (50) Wasniewski, J.; Dongarra, J.; Madsen, K.; Olesen, D., Eds. *Lecture Notes in Computer Science*; Springer-Verlag: Berlin, 1996; Vol. 1184.
- (51) Mukamel, S. *Nonlinear Optical Spectroscopy*; Oxford University Press: New York, 1995.
- (52) Hochstrasser, R. M. *Chem. Phys.* **2001**, *266*, 273.
- (53) Dreyer, J.; Moran, A.; Mukamel, S. *J. Phys. Chem. B* **2003**, *107*, 5967.
- (54) Florian, J.; Leszczynski, J. *J. Am. Chem. Soc.* **1996**, *118*, 3010.
- (55) Scheurer, C.; Piryatinski, A.; Mukamel, S. *J. Am. Chem. Soc.* **2001**, *123*, 3114.
- (56) Thompson, W. H.; Hynes, J. T. *J. Phys. Chem. A* **2001**, *105*, 2582. Kiefer, P. M.; Hynes, J. T. *J. Phys. Chem. A* **2002**, *106*, 1850.